

# Recent Advances in the Construction of 2D Heterostructures for Electrocatalytic Water Splitting

Quan Quan and Johnny C. Ho\*

Two-dimensional (2D) heterostructures, typically integrating two or more different components with well-defined interfaces, have shown great prospects in energy storage and conversion applications owing to their unique structural merits and synergistic interface effects. This review provides a comprehensive overview of the rational construction of 2D heterostructures pertaining to electrocatalytic water-splitting applications. The unique emphasis is given to the state-of-the-art progress on synthesized strategies of various well-organized 2D heterostructures. Moreover, the review offers insights into 2D heterostructures in electrocatalytic water splitting from the viewpoint of the structure–activity relationship using progressive examples. Finally, this review concludes with the potential challenges and prospects in the field, which may provide a guideline for developing more efficient 2D heterostructures to incentivize commercial implementation in this exciting research field.

## 1. Introduction

Considering the ever-growing global energy demand and environmental concerns, the search for renewable and clean energy to replace traditional nonrenewable fossil fuels is necessitated.<sup>[1]</sup>

Q. Quan, J. C. Ho  
Department of Materials Science and Engineering  
City University of Hong Kong  
Hong Kong SAR 999077, China  
E-mail: johnnyho@cityu.edu.hk

J. C. Ho  
State Key Laboratory of Terahertz and Millimeter Waves  
City University of Hong Kong  
Hong Kong SAR 999077, China

J. C. Ho  
Institute for Materials Chemistry and Engineering  
Kyushu University  
Fukuoka 816-8580, Japan

J. C. Ho  
Key Laboratory of Advanced Materials Processing & Mold  
Zhengzhou University  
Ministry of Education  
Zhengzhou 450002, China

The ORCID identification number(s) for the author(s) of this article can be found under <https://doi.org/10.1002/aesr.202200059>.

© 2022 The Authors. Advanced Energy and Sustainability Research published by Wiley-VCH GmbH. This is an open access article under the terms of the Creative Commons Attribution License, which permits use, distribution and reproduction in any medium, provided the original work is properly cited.

DOI: 10.1002/aesr.202200059

Sustainable energy sources such as wind and solar energy that can be converted into electricity are intermittent and unpredictable depending on the weather conditions in nature. For all-weather utilization, it is of paramount significance to efficiently store energy in forms of chemical energies.<sup>[2]</sup> Due to its high gravimetric energy density, zero carbon footprint emission, and recyclable merits, green hydrogen (H<sub>2</sub>) has been commonly regarded as a promising energy vector for sustainable energy systems in the future.<sup>[3]</sup> To date, it is mainly produced by energy-intensive steam methane reforming under harsh conditions accompanied by a large greenhouse gas emission load of CO<sub>2</sub>.<sup>[4]</sup> Considering the accessibility of abundant water resources on the Earth, electrocatalytic water splitting

that can convert the generated electricity into storable hydrogen with high purity under mild conditions is a captivating and scalable energy conversion technique, sustainably elevating the overall energy efficiency, whereas it is still exorbitant than traditional thermocatalytic processes based on technoeconomic analysis.<sup>[5]</sup>

In principle, in a water-splitting electrolyzer, the water dissociation process involves two half reactions: hydrogen evolution reaction (HER) on the cathode and oxygen evolution reaction (OER) on the anode, which is a thermodynamically uphill reaction.<sup>[6]</sup> Notably, the actual water-splitting process outstrips theoretical minimum thermodynamics Gibbs free energy (237.2 kJ mol<sup>-1</sup>), corresponding to a potential value of 1.23 V.<sup>[7]</sup> In this case, rational electrocatalyst design is central to facilitating reaction kinetics, especially for the suboptimum OER.<sup>[8]</sup> Currently, noble Pt-based catalysts still show benchmarking acidic HER performance with low overpotential and small Tafel slope,<sup>[9]</sup> while the Ir- and Ru-based catalysts are dominantly capitalized as state-of-the-art OER electrocatalysts owing to their robust durability.<sup>[10]</sup> However, the scarce reserves and high cost severely thwart their widespread utilization including acidic proton-exchange membranes (PEMs) and alkaline water electrolyzers (AWEs).<sup>[11]</sup> Therefore, unrelenting efforts have been devoted to low-cost acidic and alkaline HER and OER electrocatalysts, such as carbon-based nanomaterials, transition metal (TM)-based oxides, borides, carbides, nitrides, phosphides, and sulfides, alloys, and the other types.<sup>[12]</sup> However, the scientific community, governments, and industries have been vacillated because many of the aforesaid alternatives cannot offer a perfect balance among activity, cost, and stability.

Heterostructures in nanoscale, generally consisting of two or more components integrated with well-defined interfaces,<sup>[13]</sup>

have been extensively investigated to circumvent the predicament, endowing the hybrid with unique functionality and exotic properties,<sup>[14]</sup> such as the tunneling and confinement effects.<sup>[15]</sup> An effective strategy to enhance the HER/OER performance is to create appropriate heterogeneous interfaces to tailor the adsorption and desorption energies of decisive reaction intermediates to accelerate the reaction kinetics.<sup>[16]</sup> Particularly, as a propitious platform, 2D nanomaterials are promising as exemplified by graphene, owing to their large surface area, high electron transfer efficiency, and rich active sites, which are leveraged for electrochemical water-splitting reaction therein.<sup>[17]</sup> Nevertheless, it is established that in most 2D layers, defect-free basal planes alone are inactive toward the catalytic reactions.<sup>[18]</sup> Therefore, it is thoughtprovoking that the rational construction of 2D heterostructures and deuterogenic heterogeneous interfaces can provide new possibilities for optimizing the electrochemical reaction processes by adjusting the electron distribution with high-density active sites and furnishing an interfacial built-in electric field, as well as creating a strong synergism, thereby promoting the kinetics and energetics of surface catalysis.<sup>[19]</sup>

In recent years, encouraging progress has been continuously accrued in the buildout of 2D heterostructures and their applications in electrocatalytic water splitting. There have existed a number of reviews emphasizing the combinatorial strategies of heterostructures based on 2D materials as one of the building blocks hybridizing with nanoparticles, nanorods, nanocubes, and so on, which are categorized as 0D–2D,<sup>[20]</sup> 1D–2D,<sup>[21]</sup> and 3D–2D<sup>[22]</sup> based on various dimensions.<sup>[23]</sup> Thereinto, the pertinent reviews on the 2D–2D heterostructure field have mainly focused on the well-known van der Waals (vdW) heterostructures in a concentrated scope.<sup>[24]</sup> Yet, important advances identified in recent studies with respect to well-defined 2D vertical heterostructures and lateral heterostructures are not encompassed to a large extent for the electrocatalytic reactions. Therefore, a comprehensive review focusing on the multiple 2D heterostructures (such as stacking, core–shell, lateral, vertical, Janus structures, et al.) for the electrocatalytic water-splitting applications is of importance to provide researchers a better understanding on recent advances in this field.

In this review, we first concisely overview the advantages and limitations of diversified individual 2D catalysts for electrocatalytic water splitting. Then, the various synthetic strategies used to construct the heterostructures with 2D geometries are elaborately summarized, including wet-chemistry assembly, template

transformation, and epitaxial growth methods (Figure 1). In addition, we highlight recent progress in 2D heterostructures for sustainable electrocatalytic applications including HER, OER, and overall water splitting. Finally, we point out the challenges that lie ahead and propose future perspectives for the development of 2D heterostructure catalysts. This review is expected to supply inspiration and guidance for burgeoning research, which further expedites the progress of efficient electrocatalytic water electrolysis at the commercial scale.

## 2. Advantages and Limitations of Individual 2D Materials in Electrocatalysis

The unique geometry imparts 2D materials with unprecedented physical and chemical properties, which have been studied as promising platforms for multifunctional applications.<sup>[25]</sup> With the advent of graphene exfoliated from graphite via a mechanical method, the explorations of kaleidoscopic layered and nonlayered 2D nanomaterials have triggered intensive interest.<sup>[26]</sup> The typical layered 2D materials have been widely investigated up to now, including black phosphorus (BP),<sup>[27]</sup> transition metal dichalcogenides (TMDs),<sup>[28]</sup> hexagonal boron nitride (h-BN),<sup>[29]</sup> graphitic carbon nitride (g-C<sub>3</sub>N<sub>4</sub>),<sup>[30]</sup> MXenes,<sup>[31]</sup> layered metal oxides,<sup>[32]</sup> layered double hydroxides (LDHs),<sup>[33]</sup> metal–organic frameworks (MOFs),<sup>[34]</sup> covalent organic frameworks (COFs),<sup>[35]</sup> and perovskites.<sup>[36]</sup> On the other hand, the burgeoning nonlayered 2D materials have attracted incessant attention as well, encompassing metal, metal oxides, carbides, phosphides, nitrides, metal chalcogenides, perovskites, etc.<sup>[37]</sup> As is known, compared with the bulk materials, the distinctive 2D nanomaterials have been fruitfully utilized as an ideal platform for electrocatalytic applications, owing to the salient features including large surface area, affluent active sites, fast electron transfer, and tunable electronic structures at their disposal.<sup>[38]</sup>

However, “nothing” is perfect in nature. Currently, the available individual 2D nanomaterials also suffer from intrinsic limitations.<sup>[39]</sup> For instance, although graphene exhibits superior electrical conductivity and mechanical strength, it bears out only moderate catalytic performance due to the scant active sites on the surface.<sup>[40]</sup> In addition, low electrical conductivity is generally perceived as the major obstacle for some metal oxides, while serious restacking and aggregation obstruct the full utilization of their representative electrical and chemical properties.<sup>[41]</sup>

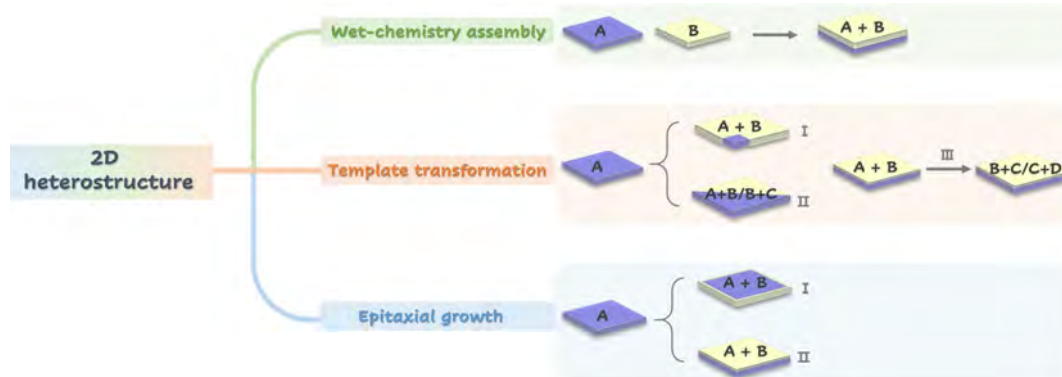


Figure 1. Schematic illustration of the synthesis of 2D heterostructures.

Moreover, the monoelemental BP material suffers from poor structural instability during the storage and reaction processes.<sup>[42]</sup> Although the electronic structure modulation of 2D nanomaterials can be tuned via surface functionalization,<sup>[15]</sup> heteroatom doping,<sup>[43]</sup> inducing defects,<sup>[44]</sup> and strain engineering<sup>[45]</sup> to optimize the adsorption energies of reactants or intermediates toward enhancing the reaction kinetics, the development of precise control strategies remains a great challenge. Alternatively, constructing heterostructures in 2D geometries through interface engineering can combine the intrinsic superiorities inherited from the individual counterparts.<sup>[46]</sup> Moreover, a synergistic effect can be achieved to optimize the catalytic performance by virtue of the exotic properties.<sup>[47]</sup> Typically, the built-in electric fields originating from the work function differences between neighboring materials can promote electron transfer.<sup>[48]</sup> In this light, an in-depth understanding of the correlation between structure and catalytic activity is imperative to develop high-efficiency electrocatalysts for water splitting in the future.

### 3. Synthetic Strategies for 2D Heterostructures

#### 3.1. Wet-Chemistry Assembly Methods

The wet-chemistry assembly method is demonstrated as a low-cost, steerable, and high-yield approach, which has been applied for massive production at present.<sup>[49]</sup> For the synthesis of 2D heterostructures, it is based on the weak vdW interlayer force or the electrostatic adsorption for restacking the well presynthesized 2D materials without the constricts of crystal lattice mismatching and occurrence of chemical transformation.<sup>[50]</sup> For example, Cheng et al. used MXene nanosheets to functionalize graphene oxide (GO) platelets through Ti—O—C covalent bonding.<sup>[51]</sup> It was indicated that Ti—O—C covalent bonding was formed at the MXene/GO heterointerface via nucleophilic substitution and dehydration reaction, which could reinforce the linking of the MXene and GO nanosheets and enhance their charge transport properties (Figure 2a–c).

LDHs are a class of typical layered materials that have attracted great attention for electrocatalytic reactions as 3d transition metals (e.g., Fe, Co, Ni) are incorporated into the host layers.<sup>[52]</sup> By taking advantages of the accessible host–guest interaction of LDHs, such as electrostatic attraction, it is easy to assemble LDHs with other 2D materials and tune the electron transfer within the 2D self-assembly to enhance the catalytic performance. For instance, Sasaki et al. assembled the exfoliated Ni–Fe LDH with graphene into a superlattice structure by electrostatic face-to-face stacking of positively charged LDH nanosheets and negatively charged graphene (oxide) in alternating sequence at a molecular scale, which creates direct interfacial contact between 3d transition metals and carbon to significantly shorten the diffusion distance (Figure 2d–f).<sup>[53]</sup> As a result, the optimal 2D heterostructure composites of Ni<sub>2/3</sub>Fe<sub>1/3</sub> LDH and GO showed outstanding OER performance in 1 M KOH aqueous solution with an overpotential of  $\approx 0.23$  V at 10 mA cm<sup>-2</sup> and Tafel slope of  $\approx 42$  mV dec<sup>-1</sup>. The activity was further improved via the heteroassembly of Ni<sub>2/3</sub>Fe<sub>1/3</sub> LDH with more conductive reduced GO (rGO) as the overpotential was reduced to  $\approx 0.21$  V and the corresponding Tafel slope to  $\approx 40$  mV dec<sup>-1</sup>.

As an emerging 2D nanomaterial, the few-layered exfoliated BP (EBP) nanosheet is also regarded as a potential electrocatalyst for various electrochemical reactions.<sup>[54]</sup> Dai et al. first produced aqueous dispersion of few-layered EBP by exfoliating the bulk sample and then constructed a new metal-free 2D heterostructure (EBP@NG) by electrostatic interaction of negatively charged ultrathin EBP and positively charged N-doped graphene (NG) (Figure 2g–i).<sup>[55]</sup> The resulting 2D heterostructure by the self-assembly method had a synergy of EBP and NG with a well-designed heterointerface, which could improve the stability of EBP and modulate the electronic structures of each component to boost their intrinsic activities. Specifically, because of the lower Fermi level of EBP relative to NG, their electronic interaction induced directional interfacial electron transfer, which not only enriched the electron density over EBP and optimized H adsorption/desorption to promote HER, but also introduced rich positively charged carbon sites on NG and provided the favorable formation of key OER intermediates (OOH\*) to improve OER energetics (Figure 2j,k). In this way, despite the poor activity for the pure EBP or NG alone, 2D EBP@NG heterostructure achieved remarkably enhanced bifunctional HER/OER activities, along with excellent durability.

Apart from the typical 2D materials (e.g., MXene, GO, LDHs, and EBP as mentioned earlier), the self-assembling of 2D MOF- and COFs-based electrocatalysts also receives extensive attention due to their tailorable pore structures and rich element-desired multielement composition.<sup>[56]</sup> Xiang et al. synthesized the 2D hybrid electrocatalysts by self-assembling pristine covalent organic polymers (COPs) with rGO (Figure 2l–n).<sup>[57]</sup> Thus, the hybridized COP/rGO materials featured significantly increased electrical conductivity, which was more than seven orders of magnitude compared with the pure COPs (from  $3.06 \times 10^{-9}$  to  $2.56 \times 10^{-1}$  S m<sup>-1</sup>). Also, the electrocatalytic performance of the 2D organic/inorganic hybrids was enhanced significantly based on the synergetic effects of highly active COP and conductive rGO.

#### 3.2. Template Transformation Methods

Template transformation strategy, based on a pre-existing nanostructured template, is one of the most effective and perspective techniques to achieve desirable high-quality topological materials. The 2D heterostructures synthesized by template-assisted synthetic strategies can hold a targeted size, shape, and composition.<sup>[58]</sup> Generally, the route for templated synthesis can be divided into the following three steps: 1) template precursor preparation; 2) template transformation by common synthesized approaches (e.g., calcination, hydrothermal reaction, precipitation, sol–gel method, and so on); and 3) template removal (if necessary) to obtain target 2D heterostructure.<sup>[59]</sup> Based on the types of templates, the template-assisted strategies can be further classified as hard-template method and soft-template method, which will be discussed respectively in this section.

##### 3.2.1. Hard-Template Method

The hard-template method is demonstrated as one of the most common strategies for the synthesis of hybrids, which is paid increasing attention to for synthesizing the electrocatalysts with

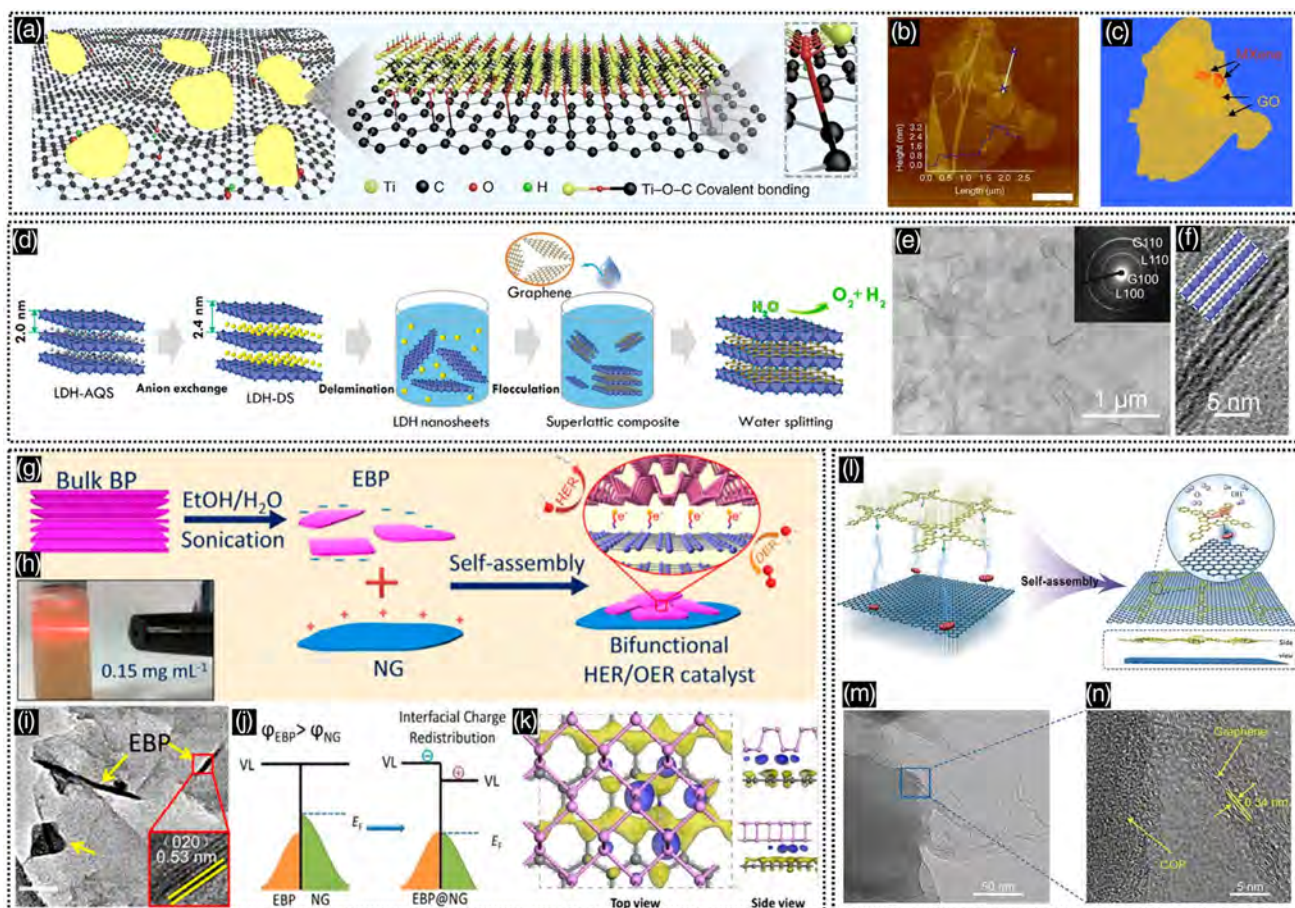


**Figure 2.** a) Schematic of the formation of MXene–GO platelets with Ti–O–C covalent bond. b) AFM image and c) corresponding illustration of the MXene–GO platelets. Reproduced with permission.<sup>[51]</sup> Copyright 2020, Springer Nature. d) Schematic illustration of heteroassembling Ni–Fe LDH nanosheets and graphene. e) TEM image (inset: corresponding selected-area diffraction [SAED] pattern) and f) HRTEM with a schematic illustration of alternately stacked LDH nanosheets and graphene. Reproduced with permission.<sup>[53]</sup> Copyright 2015, American Chemical Society. g) Schematic illustration of the liquid exfoliation of bulk BP and self-assembly with NG. h) Photograph of an EBP dispersion. i) TEM image of EBP@NG. j) Illustration of interfacial charge redistribution between NG and EBP. k) The illustrated differential charge density of NG and EBP. Reproduced with permission.<sup>[55]</sup> Copyright 2019, American Chemical Society. l) Schematic illustration of synthesis of COP/rGO. m) TEM and n) enlarged TEM images of COP/rGO. Reproduced with permission.<sup>[57]</sup> Copyright 2018, Wiley-VCH.

a desirable structure. In general, the hard template is a rigid material that can directly determine the size, structure, morphology, and components of the final sample.<sup>[60]</sup> For 2D heterostructure synthesis, the material/compound precursor with 2D geometry is usually selected as the hard template and then undergoes post-treatment with physical or chemical conversion to generate a 2D nanostructured hybrid material. For instance, based on the significantly different solubilities ( $K_{sp}$ ) between metal sulfide and hydroxide, Zhang et al. synthesized the CoNi hydroxide sheets in advance as a hard template to partially reconstruct into an ultrathin CoNi hydroxysulfide shell by an ethanol-modified surface sulfuration method, forming a 2D  $\text{Co}_{1.8}\text{Ni}(\text{OH})_{5.6}@\text{Co}_{1.8}\text{NiS}_{0.4}(\text{OH})_{4.8}$  core–shell heterostructure (Figure 3a).<sup>[61]</sup> Specifically, as the  $\text{Co}_{1.8}\text{Ni}(\text{OH})_{5.6}$  sheets were immersed in  $\text{Na}_2\text{S}$  ethanol solution under room temperature,  $\text{Co}_{1.8}\text{Ni}(\text{OH})_{5.6}$  underwent an interfacial reaction with hydrolyzed  $\text{HS}^-$  and transformed into a  $\text{Co}_{1.8}\text{NiS}_{0.4}(\text{OH})_{4.8}$  shell ( $\text{S}^{2-} + \text{C}_2\text{H}_5\text{OH} \rightarrow \text{HS}^- + \text{C}_2\text{H}_5\text{O}^-$ ,  $\text{Co}_{1.8}\text{Ni}(\text{OH})_{5.6} + \text{HS}^- \rightarrow \text{CoNi hydroxysulfide}$ ). The resultant

$\text{Co}_{1.8}\text{Ni}(\text{OH})_{5.6}@\text{Co}_{1.8}\text{NiS}_{0.4}(\text{OH})_{4.8}$  sample presented a well-maintained hexagonal plate-like morphology of the  $\text{Co}_{1.8}\text{Ni}(\text{OH})_{5.6}$  precursors with a lateral size of  $\approx 1.5 \mu\text{m}$  (Figure 3b). In this way, benefiting from the moderately regulated electronic structure, remarkably facilitated charge transfer, fully exposed active sites, and strongly coupled 2D heterointerface, the as-obtained  $\text{Co}_{1.8}\text{Ni}(\text{OH})_{5.6}@\text{Co}_{1.8}\text{NiS}_{0.4}(\text{OH})_{4.8}$  exhibited superior OER performance with an overpotential of 274.0 mV at  $10 \text{ mA cm}^{-2}$ , a low Tafel slope of  $45.0 \text{ mV dec}^{-1}$ , and favorable long-term stability.

Apart from the partial hard-template transformation as discussed earlier (symbolized as  $A \rightarrow A + B$ ), Hou et al. developed a confined carburization-engineered strategy to synthesize the novel 2D  $\text{NiO}_x/\text{Ni}$  ultrathin heterostructure nanosheets (Figure 3c), which can be exemplified as a complete hard-template transformation (symbolized as  $A + B \rightarrow C + D$ ).<sup>[62]</sup> First, ultrathin  $\text{Ni}(\text{OH})_2$  nanosheets were employed as the starting materials (Figure 3d). Then, an oxidative self-polymerization

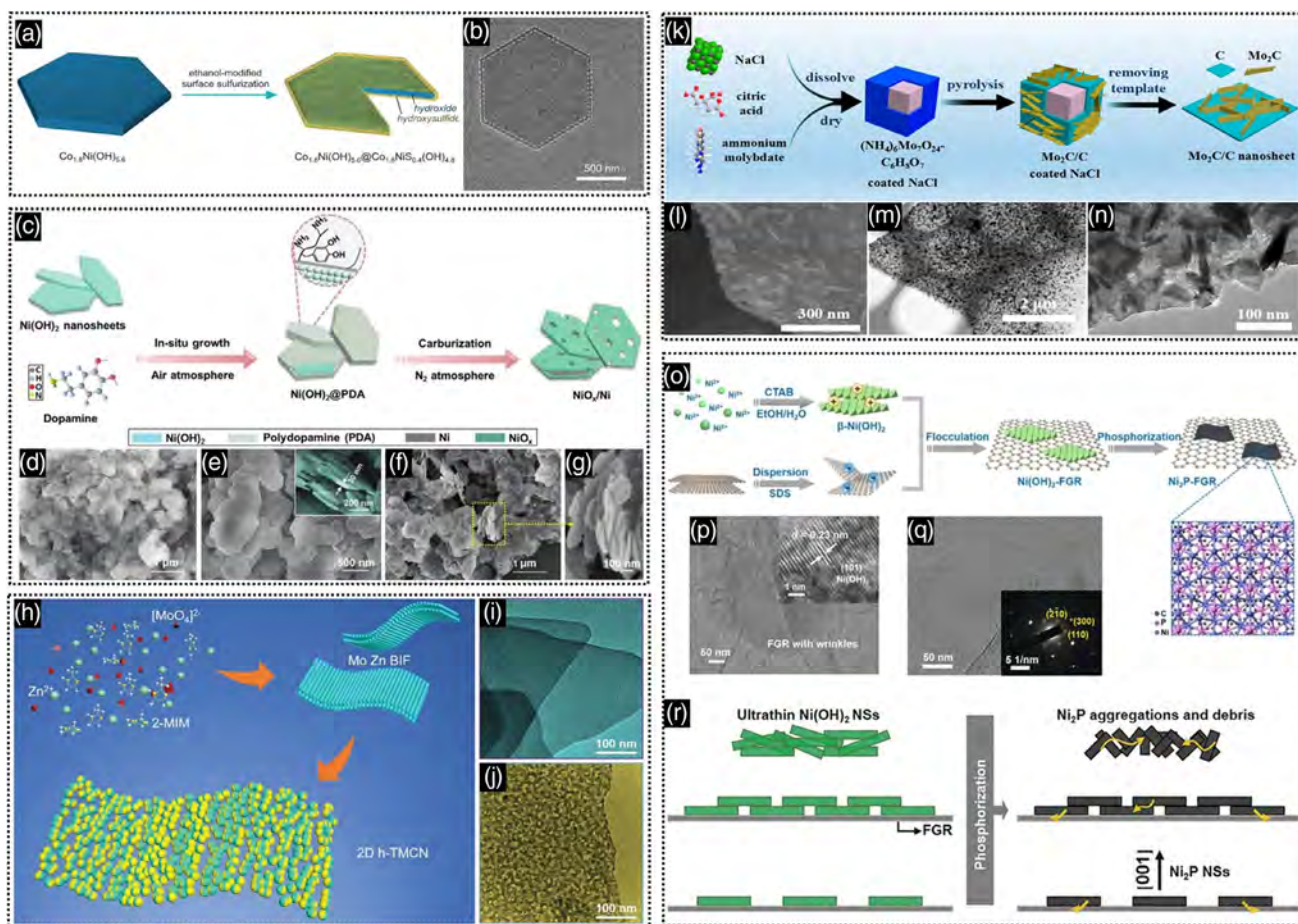


**Figure 3.** a) Schematic illustration of the fabrication of  $\text{Co}_{1.8}\text{Ni}(\text{OH})_{5.6}@\text{Co}_{1.8}\text{NiS}_{0.4}(\text{OH})_{4.8}$  core-shell heterostructures. b) TEM image of  $\text{Co}_{1.8}\text{Ni}(\text{OH})_{5.6}@\text{Co}_{1.8}\text{NiS}_{0.4}(\text{OH})_{4.8}$ . Reproduced with permission.<sup>[61]</sup> Copyright 2019, Wiley-VCH. c) Schematic diagram for the synthesis of  $\text{NiO}_x/\text{Ni}$  heterostructure nanosheets. d–f) SEM images of pure  $\text{Ni}(\text{OH})_2$ ,  $\text{Ni}(\text{OH})_2@\text{PDA}$  nanosheets, and  $\text{NiO}_x/\text{Ni}$  nanosheets, respectively (inset of (e): SEM image of side face). g) An enlarged SEM image of  $\text{NiO}_x/\text{Ni}$ . Reproduced with permission.<sup>[62]</sup> Copyright 2019, Royal Society of Chemistry. h) Schematic illustration of the synthesis of 2D h-TMCN heterostructures. TEM images of i) Mo/Zn BIF and j) 2D h-TMCN heterostructures. Reproduced with permission.<sup>[64]</sup> Copyright 2019, Wiley-VCH. k–n) Scheme of the fabrication, SEM, and TEM images of  $\text{Mo}_2\text{C}/\text{C}$  nanosheet hybrids. Reproduced with permission.<sup>[66]</sup> Copyright 2017, American Chemical Society. o) Illustration of the formation process of 2D  $\text{Ni}_2\text{P}$ -FGR heterostructure. TEM images of p) 2D  $\text{Ni}(\text{OH})_2$ -FGR and q) 2D  $\text{Ni}_2\text{P}$ -FGR (inset of (p): HRTEM image and inset of (q): SAED image). r) Schematic image showing the lattice strain transfer process from the ultrathin  $\text{Ni}_2\text{P}$  nanosheets to FGR during phosphorization. Reproduced with permission.<sup>[67]</sup> Copyright 2018, Wiley-VCH.

reaction of the dopamine precursor to polydopamine (PDA) was induced on the surface of  $\text{Ni}(\text{OH})_2$ , forming a core-shell 2D  $\text{Ni}(\text{OH})_2@\text{PDA}$  heterostructure (Figure 3e). Finally, the 2D  $\text{Ni}(\text{OH})_2@\text{PDA}$  as the hard template was subject to annealing treatment in  $\text{N}_2$  atmosphere to completely transform into 2D ultrathin  $\text{NiO}_x/\text{Ni}$  heterostructure nanosheets (Figure 3f,g). The transformation mechanism was in detail investigated. It was found that during this calcination process, as the  $\text{Ni}(\text{OH})_2$  was dehydrated into  $\text{NiO}_x$ , the carbonaceous species (e.g.,  $\text{C}_n\text{H}_{2n+2}\text{O}$ ) derived from the pyrolysis products of PDA were simultaneously diffused into the  $\text{Ni}(\text{OH})_2/\text{NiO}_x$  surface and in situ reduced the  $\text{Ni}(\text{OH})_2$  core into metallic Ni along with  $\text{CO}_x$  and  $\text{H}_2\text{O}$  gas releasing. In this work, the confined carburization strategy effectively inhibited the 2D structure from destruction with a crystal transformation so that the 2D  $\text{NiO}_x/\text{Ni}$  nanosheet heterostructures were well-defined and exhibited a superior OER performance.

Also, as the MOF family features tailorable structures and versatile compositions, 2D MOF is applied as the hard template precursor for transforming into the desirable 2D heterostructure (symbolized as  $\text{A} \rightarrow \text{B} + \text{C}$ ).<sup>[63]</sup> For instance, Wang et al. obtained the holey 2D transition metal carbide/nitride heterostructure nanosheets (h-TMCN) by controlled thermal annealing of the Mo/Zn bimetallic imidazolate frameworks (Mo/Zn BIFs) (Figure 3h).<sup>[64]</sup> Concisely, the Mo/Zn BIF precursors with 2D thin flake-like features were synthesized by the coordination and complexation of  $\text{Zn}^{2+}$ ,  $[\text{MoO}_4]^{2-}$ , and 2-methylimidazole (Figure 3i). Next, they were annealed in  $\text{N}_2$  atmosphere at 800–900 °C to enable the total pyrolysis of Mo/Zn BIF and the formation of  $\text{Mo}_2\text{C}$  and  $\text{Mo}_2\text{N}$  nanocrystals, which interlocked chemically to produce the holey 2D h-TMCN heterostructure nanoflakes (Figure 3j). Consequently, the as-prepared h-TMCN afforded low overpotentials, high turnover frequencies, and long-term cycling stability toward electrocatalytic water oxidation.

In addition, the salt template has been widely used as a typical kind of hard template, which is low cost, environmentally friendly, and easy to form and remove.<sup>[65]</sup> As illustrated in Figure 3k, Li et al. fabricated a 2D hierarchical Mo<sub>2</sub>C/C nano-sheet hybrid using a water-soluble NaCl cube crystal-template strategy.<sup>[66]</sup> This preparation process mainly involved the carburization of ammonium molybdate and citric acid on the NaCl cube crystals followed by the removal of NaCl templates. As a result, abundant sheet-like Mo<sub>2</sub>C (thickness: ≈20 nm) were uniformly anchored on the surface of carbon nanosheets (Figure 3l–n). The resultant Mo<sub>2</sub>C/C hybrids demonstrated excellent HER performance in both alkaline and acid medium with good stability, which is attributed to the strong synergistic catalytic effect and charge transfer ability. Therefore, the partial phase transformation, confined carburization reaction, controllable calcination, and salt template participation as illustrated above are the efficient shape-controlled strategies to maintain the terminal 2D nanostructural hybrids from their template precursors.

Unlike the direct self-assembly method without significant constricts of crystal lattice mismatching, to prepare the desirable 2D heterostructures, the template precursor(s) that underwent the phase transformation process could encounter the lattice strain, thus inducing structural instability. Using the self-assembly method for synthesizing a 2D heteromaterial as the hard template, the physical properties such as ductility and thermostability can be utilized to release lattice strains originating from phase transformation during the target 2D heterostructure preparation. For a typical example, Xu et al. used the electrostatic assembly of positively charged β-Ni(OH)<sub>2</sub> nanosheets and negatively charged functionalized single-layer graphene (FGR), resulting in face-to-face hybridization between Ni(OH)<sub>2</sub> and FGR.<sup>[67]</sup> Then, the Ni(OH)<sub>2</sub>-FGR heterotemplate was converted into Ni<sub>2</sub>P-FGR by a low-temperature phosphorization reaction (Figure 3o). The transmission electron microscopy (TEM) image of Ni(OH)<sub>2</sub>-FGR displayed a wrinkled sheet structure of FGR combined with ultrathin Ni(OH)<sub>2</sub> nanosheets (Figure 3p), and the TEM image of Ni<sub>2</sub>P-FGR revealed that the FGR with wrinkles was covered by ultrathin Ni<sub>2</sub>P nanosheets with ≈3.2 nm in thickness (Figure 3q). Based on the controllable experiments, the stress transfer-induced mechanism was proposed to rationalize the FGR-assisted growth of ultrathin Ni<sub>2</sub>P nanosheets from Ni(OH)<sub>2</sub> nanosheets during phosphorization (Figure 3r). It is revealed that the residual oxygenated groups (epoxy and hydroxyl groups) and lateral size of FGR contributed to interfacial bonding with ultrathin 2D Ni<sub>2</sub>P nanosheets, which facilitated stress transfer across the interface between Ni<sub>2</sub>P nanosheets with exposed (001) facets and FGR. Furthermore, the defects in FGR could be docking sites for further stabilizing 2D Ni<sub>2</sub>P nanosheets. In the absence of FGR, the single Ni<sub>2</sub>P easily forms aggregations due to the random stress transfer in the interior to reach a mechanical equilibrium.

### 3.2.2. Soft-Template Method

The soft templates mainly include macro- and microemulsions, micelles or vesicles, and some polymers as well as biological molecular assemblies.<sup>[59]</sup> The merits of the soft-template method generally include the relatively mild experimental conditions and its straightforward implementation.<sup>[68]</sup> For instance, Zhang et al.

reported the synthesis of pure hexagonal close-packed (hcp) Au square sheets (AuSSs) on GO, which was facilitated by 1-amino-9-octadecene molecules (Figure 4a).<sup>[69]</sup> The specific formation process of AuSSs on GO was as follows. 1) after mixing the 1-amino-9-octadecene and Au<sup>3+</sup> in hexane together with GO sheets, Au<sup>3+</sup> was partially reduced to Au<sup>+</sup> and complexed with 1-amino-9-octadecene; Simultaneously, 1-amino-9-octadecene–AuCl complex adsorbed onto the GO surface. 2) After ≈2 h, small Au seeds (≈2 nm) began to assemble into square-like assemblies on the GO surface. 3) The Au seeds continued to grow and fuse with one another based on a continuous supply of Au from the 1-amino-9-octadecene–AuCl complexes, finally forming the dendritic Au structures with a square-like overall morphology. The as-obtained high-quality AuSSs were indicated to be an hcp (2H type) nanostructure with an edge length between 200 and 500 nm (Figure 4b–e).

Furthermore, combining different template strategies has also been applied to construct 2D heterostructures. As a typical example, Zhuang et al. coupled soft-template with hard-template methods to synthesize targeted 2DPC-RuMo heterostructure with RuMo nanoalloy-embedded 2D porous carbon (PC) nanosheets for high-performance alkaline HER activity (Figure 4f).<sup>[70]</sup> In a typical procedure, the MgAl LDHs were first prepared to support the adsorption and further in situ polymerization of pyromellitic dianhydride (PMDA) and positively charged 1,1'-bis(4-aminophenyl)-[4,4'-bipyridine]-1,1'-dium dichloride (Vio-NH<sub>2</sub>·2Cl<sup>−</sup>) on their outer surfaces, thus forming an ionic polyimide-coated LDH (IPI-Cl@LDH). After an anion-exchange process, the initial chloride anions in IPI-Cl@LDH were replaced by metal-containing anions, such as MoO<sub>4</sub><sup>2−</sup> and Ru(CN)<sub>6</sub><sup>4−</sup>, yielding a metal-atom-containing polyimide-coated LDH (IPI-X@LDH). Undertaking a further calcination treatment, the polyimides with bimetal-containing counter anions converted to 2DPC-RuMo, while the inner LDH template changed into layered double oxide (LDO), allowing the formation of 2DPC-RuMo@LDO. With further etching of LDO templates, the target 2DPC-RuMo nanosheets were obtained, possessing RuMo nanoalloy domains on the hexagonal carbon nanosheets (Figure 4g–m).

## 3.3. Epitaxial Growth Methods

Epitaxial growth refers to the deposition of crystalline material on the well-defined surface of a crystalline substrate, where the overlayer has the same crystalline orientation as the substrate material.<sup>[71]</sup> Epitaxial growth of hybrid nanostructures is a precisely controlled synthesis approach to achieve desired constitution, composition, crystal phases, and exposed facets and/or interfaces.<sup>[72]</sup> Considering epitaxial orientation, we classify the epitaxial growth method into lateral growth and vertical growth for 2D heterostructure synthesis in this section.

### 3.3.1. Lateral Growth

Lateral growth is the directional growth of a second material at the edge of an existing domain of a first material. As a typical example in Figure 5a, Duan et al. applied a chemical vapor deposition (CVD) method for the robust epitaxial growth of lateral

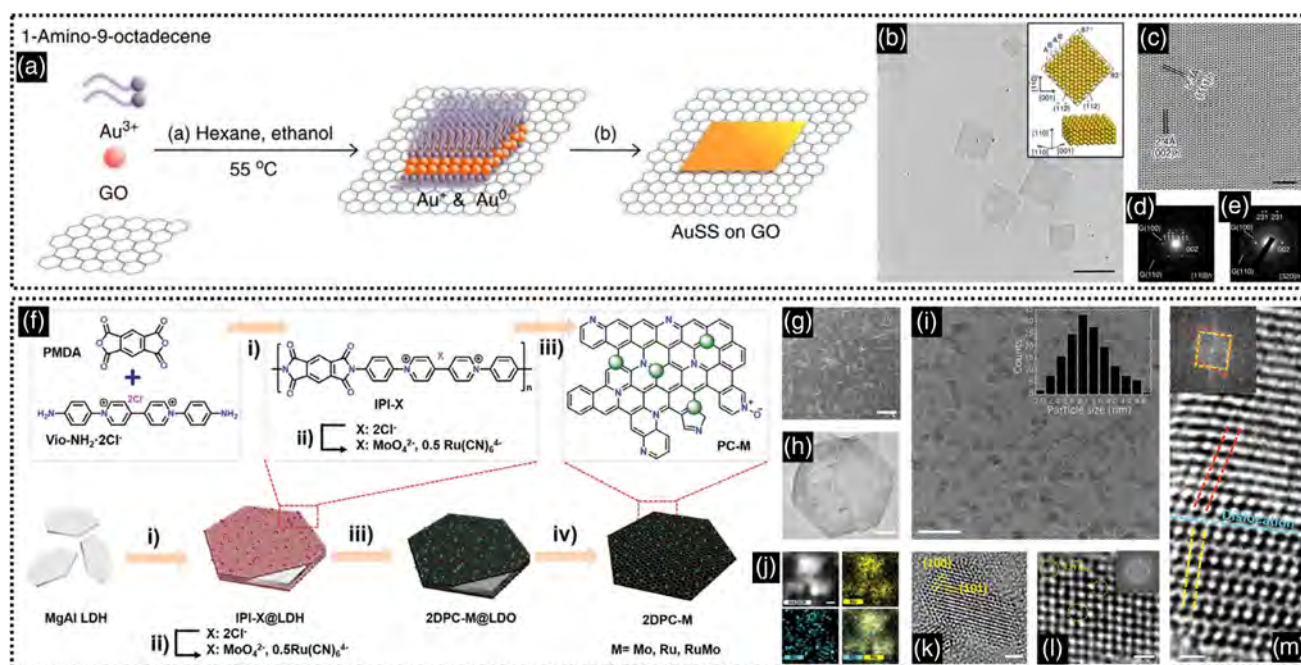


**Figure 4.** a) Schematic illustration of the formation process of Au SS on GO. b,c) TEM and HRTEM images of AuSSs on a GO surface; d,e) SAED patterns of AuSSs on GO sheets from  $[110]_h$  and  $[320]_h$  zone axis. Reproduced with permission.<sup>[69]</sup> Copyright 2011, Springer Nature. f) Scheme of the fabrication procedure for 2DPC–RuMo nanosheets. g) SEM image of the obtained 2DPC nanosheets. h,i) TEM and HRTEM images of 2DPC–RuMo nanosheets. j) HAADF–STEM and EDS elemental mappings of RuMo–nanoalloy particles on the hexagonal carbon nanosheets. k,l) HRTEM images of RuMo nanoalloy in 2DPC–RuMo nanosheets (inset: corresponding fast Fourier transform [FFT] image). m) HRTEM image of a grain boundary with distinct dislocations. Reproduced with permission.<sup>[70]</sup> Copyright 2020, Wiley-VCH.

heterostructures based on the 2D atomic crystals of the TMD family (e.g.,  $\text{MoS}_2$ ,  $\text{MoSe}_2$ ,  $\text{WS}_2$ , and  $\text{WSe}_2$ ).<sup>[73]</sup> Figure 5b shows the optical microscope images of the synthesized triangular domains of a wide range of monolayer heterostructures, including  $\text{WS}_2$ – $\text{WSe}_2$ ,  $\text{WSe}_2$ – $\text{MoS}_2$ ,  $\text{WS}_2$ – $\text{MoS}_2$ ,  $\text{WSe}_2$ – $\text{MoSe}_2$ , and  $\text{WS}_2$ – $\text{MoSe}_2$  on  $\text{SiO}_2/\text{Si}$  substrates, which all exhibited two concentric regions with slightly different optical contrast (Figure 5c). More complex compositionally modulated lateral multiheterostructure superlattices ( $\text{WS}_2$ – $\text{MoS}_2$ – $\text{WS}_2$ ,  $\text{WS}_2$ – $\text{WSe}_2$ – $\text{MoS}_2$ , and  $\text{WS}_2$ – $\text{MoSe}_2$ – $\text{WSe}_2$ ) and lateral superlattices ( $\text{WS}_2$ – $\text{WSe}_2$ – $\text{WS}_2$ – $\text{WSe}_2$ ) can be synthesized on  $\text{SiO}_2/\text{Si}$  substrates while tuning the number of periods and repeated spacing varied through a step-by-step growth process. Such 2D lateral heterostructures epitaxially grown on a substrate can be used in electrochemical applications by rational transformation techniques.

However, such 2D lateral heterostructures obtained from the traditional CVD method have low yield as electrocatalysts and need harsh synthetic conditions (e.g., high temperature, vacuum). On the contrary, the lateral epitaxial growth in a liquid phase is an approach to synthesizing the 2D heterostructure catalysts on a larger scale at low temperatures, which is widely used for electrocatalytic applications. For instance, Zhang et al. synthesized a lateral MOF/MOF heterostructure by a wet-chemistry method (Figure 5d).<sup>[74]</sup> Specifically, Zr–BTB (BTB = benzene tribenzoate) nanosheets grow faster on the edges of PCN-134 nanoplates through coordination of BTB ligands with metal nodes than their growth on the basal planes of PCN-134, leading to selective growth of Zr–BTB on the edges of PCN134 nanoplates, which have been confirmed by their scanning electron microscopy

(SEM), scanning transmission electron microscopy (STEM), and high-angle annular dark-field STEM (HAADF–STEM) images (Figure 5e–g). In addition, Yu et al. prepared a lateral BP/dicobalt phosphide (BP/ $\text{Co}_2\text{P}$ ) heterostructure by a solvothermal strategy, in which  $\text{Co}_2\text{P}$  was edge selectively grown on BP nanosheets.<sup>[75]</sup> The BP nanosheets were first obtained by liquid exfoliation with defects inevitably produced. According to the first-principles calculation, the defect occupation energy of Co (7.65 eV) was lower than the surface adsorption energy (4.41 eV) so that Co ions were easily reduced to Co atoms on the defect sites. The generated Co atoms tended to bond with adjacent P atoms. Therefore, the lattice rearrangement, crystallization, and continuous ripening of  $\text{Co}_2\text{P}$  took place (Figure 5h). As the unsaturated P and defects were usually enriched on the BP edges, the formation of  $\text{Co}_2\text{P}$  tended to take place at the edges (Figure 5i,j). As a result, the edge-occupied  $\text{Co}_2\text{P}$  provided effective electrocatalytic sites to improve the electrocatalytic activities for HER and OER.

In addition, our group coupled the lateral growth method and hard-template transformation to synthesize 2D metal phosphide loop-sheet heterostructures (Figure 5k).<sup>[76]</sup> First, we edge selectively grew the Ni–Fe PBA nanocubes along the periphery of ultrathin  $\text{Ni}(\text{OH})_2$  nanosheets by controlling the coordination reaction kinetics, constructing a 2D loop-sheet heterostructure as a hard template (Figure 5l). In the next phosphorization step, the edge-loop topology was found to compensate for the stress induced in the phase transformation process. In this case, the obtained metal phosphides were well maintained with their 2D heterostructure, in which the interconnected polycrystalline

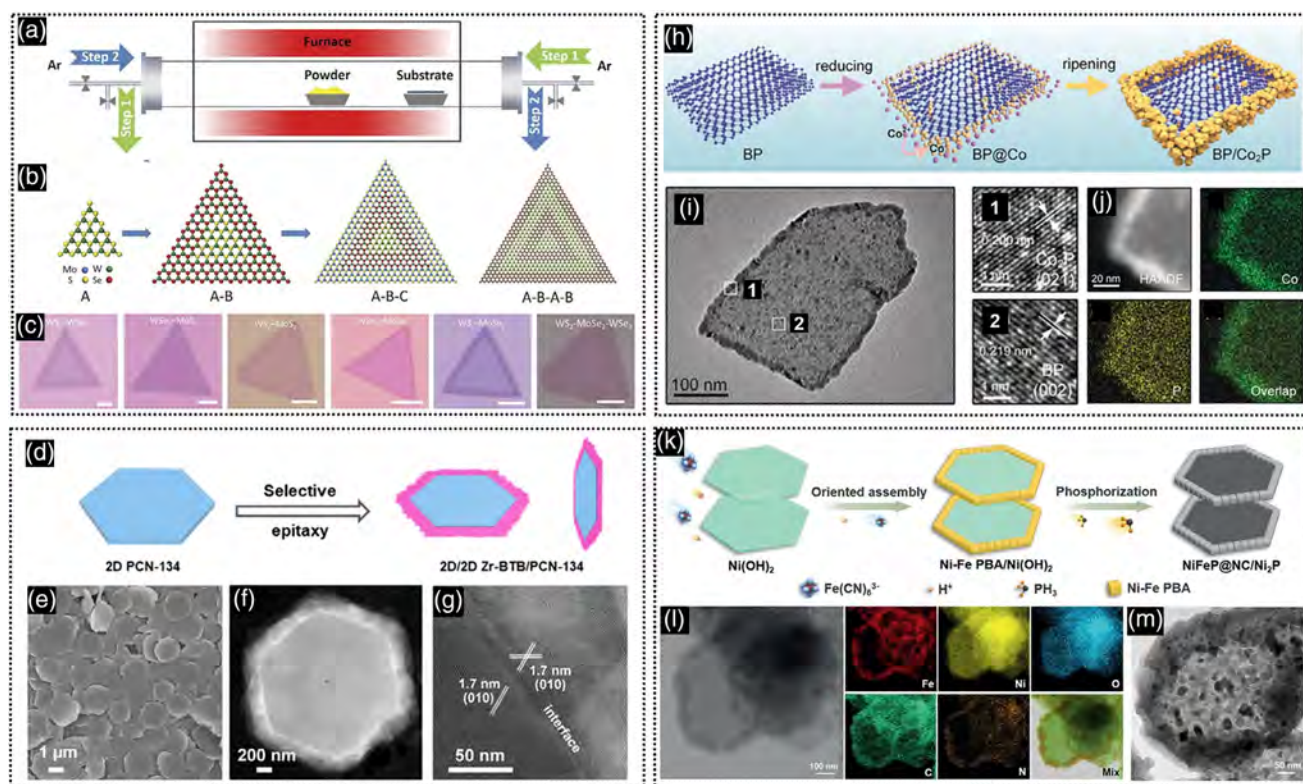


**Figure 5.** a, b) Schematic illustration of the epitaxial growth of lateral heterostructures and the models of A, A-B, A-B-C, and A-B-A-B heterostructures. c) Optical microscope image of  $WS_2$ - $WSe_2$ ,  $WSe_2$ - $MoS_2$ ,  $WS_2$ - $MoS_2$ ,  $WSe_2$ - $MoSe_2$ ,  $WS_2$ - $MoSe_2$ , and  $WS_2$ - $MoSe_2$ - $WSe_2$  heterostructures. Reproduced with permission.<sup>[73]</sup> Copyright 2017, American Association for the Advancement of Science. d) Schematic diagram of the synthesis of Zr-BTB/PCN-134 heterostructure. e-g) SEM, STEM, and HAADF-STEM images of 2D Zr-BTB/PCN-134 heterostructure. Reproduced with permission.<sup>[74]</sup> Copyright 2020, American Chemical Society. h) Schematic illustration of the synthesis process of the 2D BP/ $Co_2P$  heterostructure. i) TEM and HRTEM images and j) HAADF-STEM image and EDS mapping of BP/ $Co_2P$  nanosheet. Reproduced with permission.<sup>[75]</sup> Copyright 2018, Wiley-VCH. k) Schematic figure of the synthesis of NiFeP@NC/ $Ni_2P$  loop-sheet heterostructures. l) STEM-EDS element mapping of Ni-Fe PBA/ $Ni(OH)_2$ . m) TEM image of NiFeP@NC/ $Ni_2P$ . Reproduced with permission.<sup>[76]</sup> Copyright 2021, Wiley-VCH.

$Ni_2P$  nanoparticles as sheet structures were edge confined by the N-doped carbon loop containing ultrafine uniform NiFeP nanocrystals (denoted as NiFeP@NC/ $Ni_2P$ ) (Figure 5m). This loop-sheet feature with lifted edges prevented the stacking of nanosheets and induced accessible open channels for catalytic site exposure and gas bubble release, which contributed to a remarkable OER activity.

### 3.3.2. Vertical Growth

Opposite to lateral growth, vertical growth is the basal surface directional growth of a second material on a first 2D material. The  $WSe_2$ / $SnS_2$  bilayer heterostructure is a typical example of vertical growth, which was synthesized by a two-step CVD strategy (Figure 6a-c).<sup>[77]</sup> 1) The large-scale  $WSe_2$  monolayers were grown on the  $SiO_2$ / $Si$  substrate through a CVD process (Figure 6d). 2) vdW epitaxial growth of  $SnS_2$  monolayers in the vapor phase took place on the  $WSe_2$  monolayers to achieve the vertical bilayer heterostructures (Figure 6e).

In addition, Huang et al. developed a solution-phase epitaxy strategy to obtain vertical  $Sn_{0.5}W_{0.5}S_2$ / $SnS_2$  heterostructures (Figure 6f).<sup>[78]</sup> The  $SnS_2$  nanoplates were first synthesized *via*

a hydrothermal reaction. Then,  $(NH_4)_{10}H_2(W_2O_7)_6$  was added to the  $SnS_2$  solution, keeping it at 220 °C for 60 h. During this process, the  $Sn_{0.17}WO_3$  nanorods were formed at the beginning of the hydrothermal reaction and then gradually decomposed at 220 °C, providing additional Sn and W ions with a high W/Sn ratio (>30) to drive the growth of alloyed  $Sn_{0.5}W_{0.5}S_2$  nanosheets on the surface of  $SnS_2$ . As a result, the alloyed  $Sn_{1-x}W_xS_2$  nanosheets were in situ synthesized and hybridized with  $SnS_2$  nanoplates (Figure 6g,h). Especially, the side-view TEM image in Figure 6i showed an  $SnS_2$  nanoplate covered by  $Sn_{1-x}W_xS_2$  nanosheets on both its basal faces forming a vertical heterostructure.

Besides the TMDs-based vertical heterostructure, the ultrathin graphdiyne (GDY) layers were reported to controllably grow on the surface of cobalt nitride nanosheets ( $CoN_x$  NSs) through crosscoupling reaction, forming the  $CoN_x$ @GDY NS heterostructure (Figure 6j-m).<sup>[79]</sup> The surface growth of GDY had rich  $C\equiv C$  triple bonds and chemical and mechanical robustness, which were beneficial to adsorb water molecules and could protect the whole electrocatalyst from degradation. Therefore,  $CoN_x$ @GDY NS heterostructure exhibited superior activities and long-term stabilities toward HER and OER.

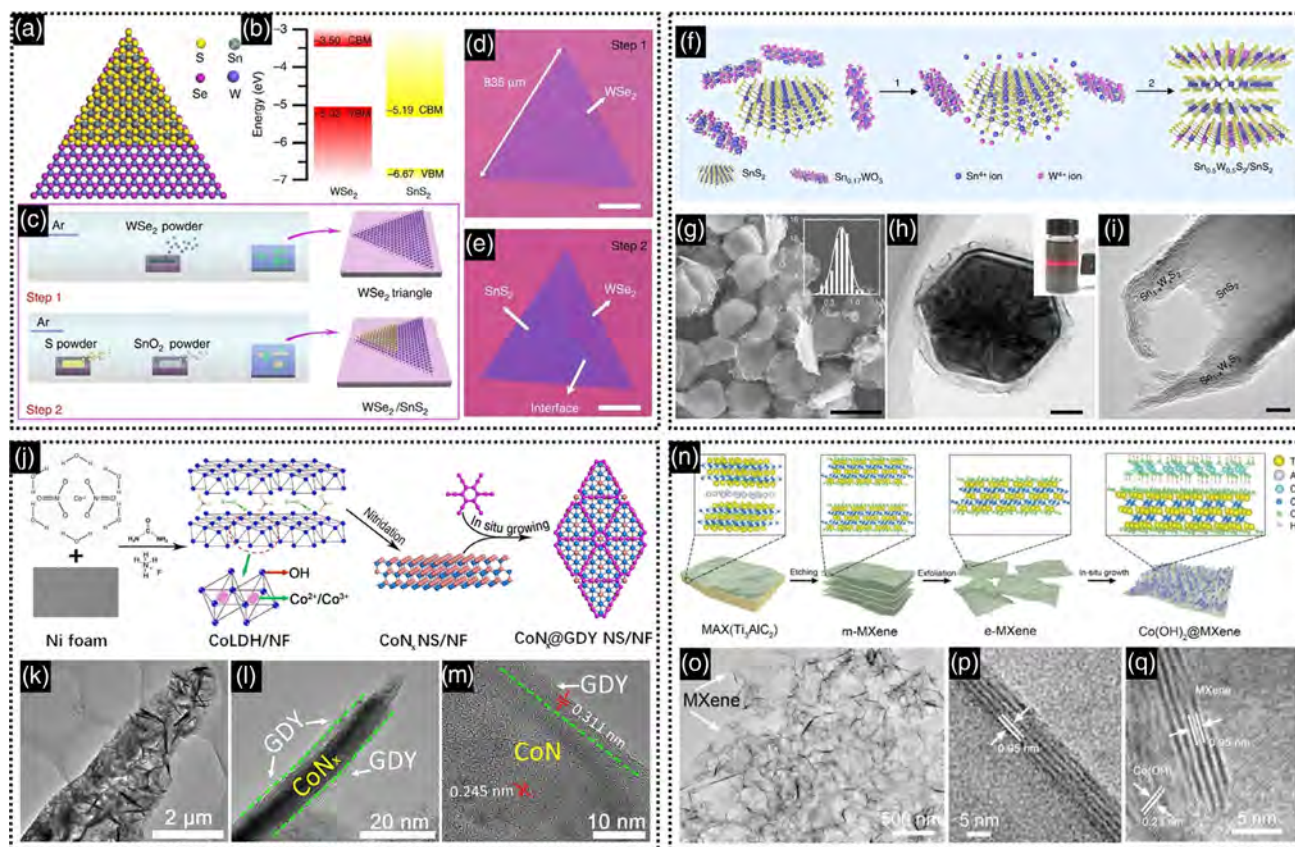


**Figure 6.** a,b) Structure model and band alignment of vertically stacked  $\text{WSe}_2/\text{SnS}_2$  heterostructure. c) Schematic illustrating the epitaxy growth of  $\text{WSe}_2$  triangular flake and  $\text{WSe}_2/\text{SnS}_2$  heterostructure. d,e) Corresponding typical optical images. Reproduced with permission.<sup>[77]</sup> Copyright 2017, Springer Nature. f) Schematic illustration of the preparation of  $\text{Sn}_{0.5}\text{W}_{0.5}\text{S}_2/\text{SnS}_2$  heterostructures. g–i) SEM and top-view and side-view TEM images of typical  $\text{Sn}_{1-x}\text{W}_x\text{S}_2/\text{SnS}_2$  heterostructures (inset of (h): photograph of a solution showing the Tyndall effect). Reproduced with permission.<sup>[78]</sup> Copyright 2018, Springer Nature. j) Schematic diagram of the synthesis of 2D  $\text{Co}_x\text{@GDY}$ . k–m) TEM and HRTEM images of  $\text{Co}_x\text{@GDY}$ . Reproduced with permission.<sup>[79]</sup> Copyright 2019, Elsevier. n) Schematic figure for the synthesis process of  $\text{Co}(\text{OH})_2\text{@MXene}$  hybrids. o–q) TEM and HRTEM images of  $\text{Co}(\text{OH})_2\text{@MXene}$ . Reproduced with permission.<sup>[80]</sup> Copyright 2021, Royal Society of Chemistry.

Moreover, Peng et al. designed a series of transition-metal hydroxides@MXene (TMHs@MXene) hierarchical hybrid architectures, including  $\text{Co}(\text{OH})_2\text{@MXene}$ ,  $\text{Ni}(\text{OH})_2\text{@MXene}$ , and  $\text{FeOOH@MXene}$ , by in situ growing interconnected ultrathin TMH networks on the surface of  $\text{Ti}_3\text{C}_2\text{T}_x$  MXene nanosheets (Figure 6n).<sup>[80]</sup> First, the accordion-like  $\text{Ti}_3\text{C}_2\text{T}_x$  structure was obtained by  $\text{LiF}/\text{HCl}$  selective-etching process, and then the few-layer ultrathin  $\text{Ti}_3\text{C}_2\text{T}_x$  MXene nanosheets were prepared by ultrasonic exfoliation. After that, by mixing the metal salt solution with a well-dispersed MXene suspension, TMH nanostructures are in situ grown on the surface of MXene nanosheets. The presence of abundant terminal groups ( $-\text{O}$ ,  $-\text{OH}$ , et al.) on the MXene surface enabled the easy adsorption of metal cations. Taking  $\text{Co}(\text{OH})_2\text{@MXene}$  as an archetype, the TEM and high-resolution TEM (HRTEM) images revealed that the sheet-like  $\text{Co}(\text{OH})_2$  subunits homogeneously covered the surface of ultrathin MXene layers to form a 2D/2D heterojunction (Figure 6o–q). The unique hybrid structure and strong interfacial interaction provided sufficient active sites and robust structure, thus ensuring favorable electrochemical kinetic and superior Pt-like HER catalytic activity.

### 3.4. Advanced Approaches for Characterizing 2D Heterostructures

Advanced characterization techniques are indispensable to the gain of high-quality 2D heterostructures. For example, microscopic characterization techniques, including SEM, TEM, and STEM, are the most direct ways to observe the morphology (i.e., size, shape, or thickness) while the additional energy-dispersive X-ray (EDX) and electron energy loss spectrum (EELS) are applied to explore the component distribution. Especially, the contact types and heterointerfaces of 2D heterostructure materials can be explored at the nanoscale level by HRTEM besides the conventional structural parameters, such as crystallinity, phase, and exposed facets.<sup>[81]</sup> Moreover, atomic force microscopy (AFM) is the most widely used high-resolution surface imaging technique to evaluate the morphology (size, thickness, or wrinkle) of 2D nanomaterials while the different components can be further discerned based on the quantitative information on surface roughness.<sup>[82]</sup> In addition, Kelvin probe force microscopy (KPFM) as a variant of the AFM technique can distinguish various components in 2D

heterostructures by the analysis of the local contact potential difference.

X-ray photoelectron spectroscopy (XPS) is a powerful spectroscopic technique to determine the chemical composition and surface oxidation states of a hybrid material.<sup>[83]</sup> For specific cases, the sputtering technique can be used to investigate the stacking or core-shell 2D heterostructures. X-ray absorption spectroscopy (XAS), also known as X-ray absorption fine structure spectroscopy (XAFS) divided into two regimes including X-ray absorption near-edge structure (XANES) and extended X-ray absorption fine structure (EXAFS), is paid increasing attention to as a sensitive nondestructive and element-specific spectroscopic technique, which can probe the structure characteristics of nanomaterials at the atomic scale (e.g., the oxidation state, coordination chemistry, bond length, and species of the atoms). For the exploration of 2D heterostructures, XAFS is an efficient approach to assess the local atomic arrangements, electronic structures, and interactions between different components.<sup>[84]</sup> Furthermore, according to the unique optical, electrical, magnetic, and other properties of the individual component, the properties of 2D assembles can be preferably expounded by relevant physicochemical characterization methods, such as optical image, Raman spectroscopy, Mössbauer spectroscopy, and electrochemical techniques. The clear and accurate characterizations for 2D heterostructures are of significant importance in understanding the structure–functionality relationship, as well as in providing a guideline to rationally design the highly efficient 2D heterostructures for the target electrocatalytic applications.

## 4. 2D Heterostructures for Electrocatalytic Water Splitting

### 4.1. 2D Heterostructures for HER

HER from water electrolysis is well suited for establishing a clean, emission-free, and cost-effective renewable route for the bulk generation of H<sub>2</sub> as the energy carrier.<sup>[85]</sup> At present, metal platinum (Pt) is still the benchmarking electrocatalyst for HER, but the high cost and limited reserves commercially hinder its practical applications.<sup>[86]</sup> In this regard, to drive the cost of H<sub>2</sub> production from water electrolysis down, it is of significant importance to decrease the Pt loading and increase the Pt utilization efficiency.<sup>[87]</sup> Downsizing the Pt nanoparticles to clusters or even single atoms is an effective pathway to decrease noble metal usage and increase their catalytic activity.<sup>[88]</sup> In addition, interfacing Pt nanocrystals (NCs) with metal-based materials can be another facile method to further exert the high efficiency of Pt for HER under the synergistic effects.

For instance, the installation of a nanometer-thick 2D Pt layer on the Ni(OH)<sub>2</sub> nanosheet surface could build the maximized area of the intimate Pt/Ni(OH)<sub>2</sub> heterointerface along the 2D developed commissure plane. In addition, the ultrathin 2D Pt catalyst would offer the highest exposure of active sites and a substantially shortened pathway for charge transfer and mass diffusion to achieve superior Pt atom utilization and better long-term stability. As a proof of concept, Lee et al. developed the confined in-solution growth of 2D Pt-extended islands of basal area coverage on the LDH-based functional template (LDH@2D-Pt)

(Figure 7a).<sup>[89]</sup> Specifically, an aqueous colloidal suspension of NiFe-LDHs was mixed with solutions of Na<sub>2</sub>PtCl<sub>4</sub> and ascorbic acid, which was maintained under acidic pH 3.5 and a temperature of 70 °C. The as-obtained products were designated as A-LDH/2D-Pt. As shown in Figure 7b, the growth of Pt was strictly confined within the 2D plane of NiFe-LDH, resulting in mono-dispersed hexagonal lamellar Pt sheet-like structures with an overall lateral size of 120 ± 20 nm. It was indicated that the average thickness of an isolated sheet of A-LDH/2D Pt was ≈9.6 nm, with ≈1.5 nm thickness of the 2D Pt grown on each side of the LDH sheet. In addition, the N-LDH/2D Pt sample was synthesized with Pt growth conducted at neutral pH conditions to ensure the stability of the LDH component.

The HER activities of N-LDH/2D Pt, A-LDH/2D Pt, 2D Pt [LDH + 2D Pt] (physical mixture with 1:1 weight content), and 20% Pt/C were evaluated in 1.0 M KOH solution in a standard three-electrode system. As a result, N-LDH/2D Pt needed 61 mV overpotential ( $\eta_{100}$ ) to reach as high as 100 mA cm<sup>-2</sup>, which was significantly lower than A-LDH/2D Pt ( $\eta_{100}$  = 111 mV), 2D Pt ( $\eta_{100}$  = 165 mV), [LDH + 2D Pt] ( $\eta_{100}$  = 173 mV), and 20% Pt/C ( $\eta_{100}$  = 342 mV) at same current density (Figure 7c). N-LDH/2D Pt exhibited an almost unchanged linear sweep voltammetry (LSV) profile with merely 11 mV rise in overpotential to attain 100 mA cm<sup>-2</sup> after 5000 cyclic voltammetry (CV) cycles, indicating good stability for N-LDH/2D Pt (Figure 7d). In addition, N-LDH/2D Pt exhibited stable chronopotentiometric (CP; at 10 mA cm<sup>-2</sup>) and chronoamperometric (CA; -0.05 V vs. reversible hydrogen electrode) curves for 50 h of electrolysis. In a word, such LDH@2D-Pt heterostructures featured the well-engineered 2D–2D tight interface and synergistically integrated active sites on NiFe-LDH and porous ultrathin Pt layer, contributing to the superior HER performance and decent stability (Figure 7e).

Actually, owing to their low cost and abundant storage, the TM-based compounds, such as TM-based oxides,<sup>[90]</sup> disulfides,<sup>[91]</sup> phosphides,<sup>[92]</sup> carbides,<sup>[93]</sup> and nitrides,<sup>[94]</sup> are regarded as the alternatives to the expensive noble metal catalysts. Moreover, the 2D TM-based heterostructures featuring high specific surface area are desirable structures for the liquid-phase electrocatalytic reaction by fully exposing accessible surfaces and active sites.<sup>[95]</sup> The unique d-band center of transition metals can be tuned by the topologies and the components within the hybrids, which further optimize their electrocatalytic performance. For example, Hou et al. produced a 2D hybrid electrocatalyst consisting of a Mo-doped WC core embedded within N-doped carbon shells (NCS) through carbonization treatment on a 2D MOF template precursor.<sup>[96]</sup> Owing to the large surface area, the as-obtained Mo-WC@NCS exhibited good and robust HER performance in alkaline, acid, and neutral media (Figure 7f–h). The theoretical calculations demonstrated that the d-band center of W in the Mo-WC@NCS hybrid was downshifted after Mo dopants, which was beneficial to modulating the electronic structure of W centers, and thereby facilitated H desorption to boost hydrogen generation (Figure 7i–k).

### 4.2. 2D Heterostructures for OER

OER, as another half reaction at the anode of water splitting, suffers from a kinetically sluggish four-electron-transfer process.<sup>[97]</sup>

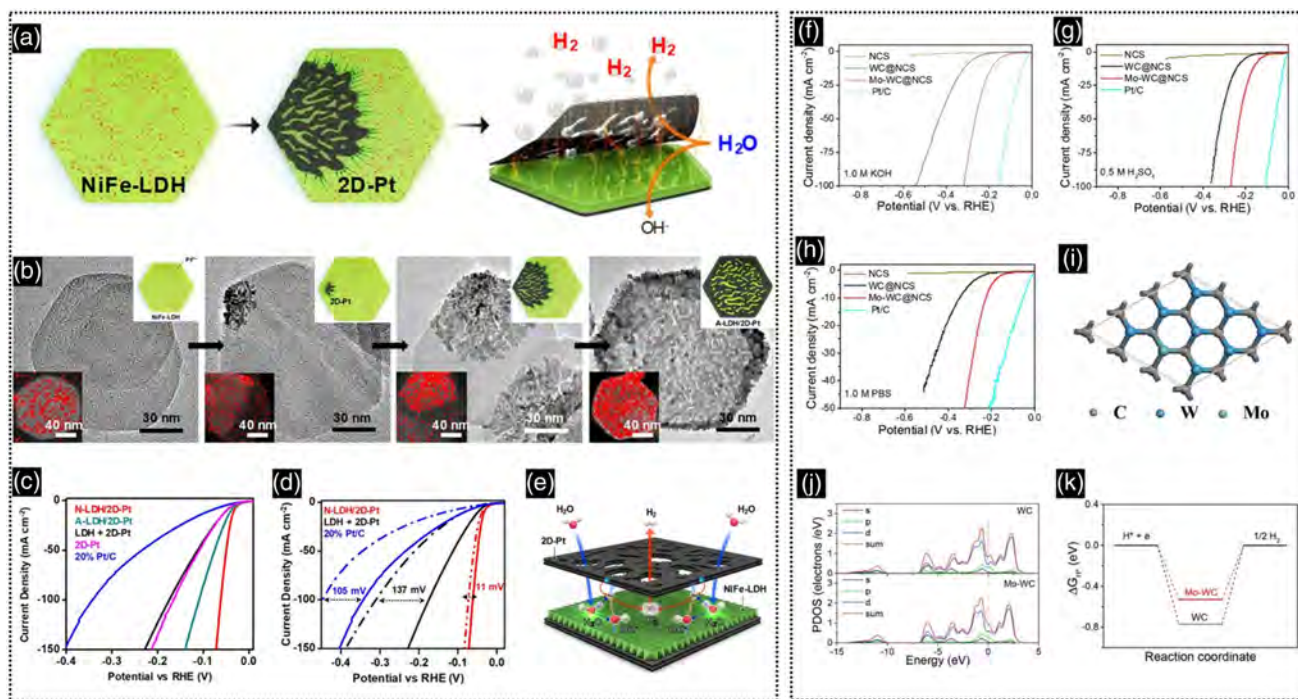


**Figure 7.** a) Schematic illustration of the synthesis of 2D Pt on LDH for HER. b) The corresponding TEM and HAADF–STEM images with EDS elemental mapping for Pt for various intermediates and the final product. c) IR-corrected LSV profiles and d) profiles after the cyclic stability test. e) Schematic figure of facilitated HER mechanism at the heterointerface. Reproduced with permission.<sup>[89]</sup> Copyright 2020, American Chemical Society. Polarization curves in f) alkaline, g) acid, and h) neutral media. i) Geometric configuration of 2D Mo–WC (001) with Mo atoms replacing the subsurface W atoms. j) Calculated partial density of states (PDOS) of W atom in WC (001) and Mo–WC (001). k) HER free energy diagrams for WC and Mo–WC. Reproduced with permission.<sup>[96]</sup> Copyright 2020, Elsevier.

2D heterostructures have emerged as promising and efficient electrocatalysts for OER based on their unique structural and chemical properties.

Zhu et al. synthesized 2D FeCo LDH/CoO nanosheets as hard templates and then transferred them into Fe-containing CoP/CoO nanosheets by selective low-temperature phosphorization.<sup>[98]</sup> The as-prepared 2D Fe–CoP/CoO heterostructure configured with logical component design and in-plane component tunability exhibited a strong interfacial coupling effect, contributing to a superior OER performance with an overpotential of 219 mV at a current density of  $10 \text{ mA cm}^{-2}$  (Figure 8a). The CP test of Fe–CoP/CoO exhibited high stability for 12 h at  $10 \text{ mA cm}^{-2}$  in 1.0 M KOH solution. Meanwhile, the polarization curve of Fe–CoP/CoO showed a negligible difference after 3000 CV cycles compared with the original data, further demonstrating its good stability (Figure 8b). Toward good performance and stability, density functional theory (DFT) calculations were further conducted to probe the interfacial mechanism. The compared results for density of states (DOS) and charge density distribution of CoP and Fe–CoP indicated that the introduction of Fe was favorable for charge carrier transfer during the OER process (Figure 8c,d). In addition, the oxygen in CoP/CoO interfaces decreased the Gibbs free energy of  $\Delta G_2$  from 1.75 to 1.40 eV and significantly changed the rate-determining step from step 2 ( $\Delta G$  (\*O)) to step 3 ( $\Delta G$  (\*OOH)) compared with pure CoP. The incorporation of Fe further optimized the Gibbs free energy of the

rate-determining step 3 from 1.71 to 1.64 eV, inducing OER much easily compared with pure CoP/CoO (Figure 8e).

The above results demonstrate that the construction of 2D heterostructure can optimize the heterointerfaces to modulate electronic structure, increase charge carrier densities, and decrease Gibbs free energies to accelerate the OER efficiency. Besides the explorations of the structure–function relationship, increasing attention is placed on the in-depth mechanism exploration for OER based on advanced characterizations.<sup>[99]</sup>

Song et al. prepared iridium (Ir) as clusters and single atoms incorporated into the defect-rich cobalt-based hydroxide nanosheets (nominated as CoIr) for OER (Figure 8f).<sup>[100]</sup> The optimized CoIr with 9.7 wt% Ir content (nominated as CoIr-0.2) displayed highly efficient OER performance with an overpotential of 373 mV at  $10 \text{ mA cm}^{-2}$  in 1.0 M phosphate buffer solution (Figure 8g). In addition, the CoIr-0.2 sample also required a low overpotential of 235 mV to reach  $10 \text{ mA cm}^{-2}$  in 1.0 M KOH for OER. The good durability of CoIr-0.2 was confirmed by the stable CP tests at  $10 \text{ mA cm}^{-2}$  for 10 h in both neutral and alkaline solutions. The XAFS spectroscopy toward CoIr-0.2 after OER indicated the transformation of  $\alpha\text{-Co(OH)}_2$  to  $\beta\text{-CoOOH}$  phase on the CoIr-0.2 sample surface and the formation of high-valence Ir species with low-coordination structure due to high oxidation potentials (Figure 8h–j), which were the real catalytic active sites for the OER activity. Furthermore, Hou et al. grew Ce-doped Ni-based MOF on the surface of oxygen-functionalized electrochemically

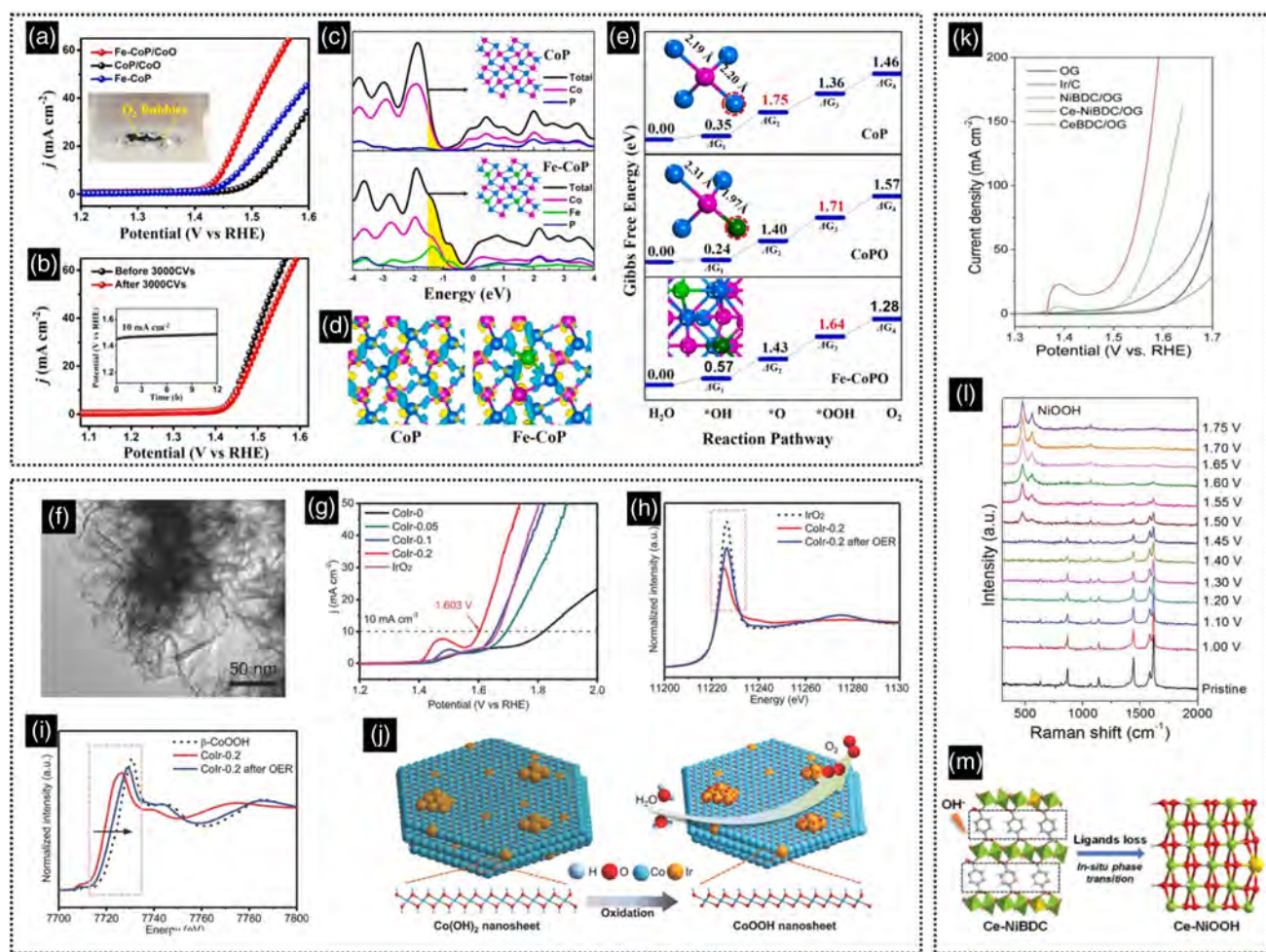


**Figure 8.** a) Polarization curves for OER and b) the curves of 2D FeCoP/CoO before and after 3000 CV cycles (inset: the chronopotentiometry curve). c) Calculated total and partial DOS for CoP and Fe-CoP d) The charge density distributions. e) The standard free energy diagram and calculated rate-determining steps of the OER process on the CoP, CoPO, and Fe-CoPO surfaces, respectively. Reproduced with permission.<sup>[98]</sup> Copyright 2018, Elsevier. f) TEM image of 2D Colr-0.2. g) LSV curves for OER. h) Ir L<sub>3</sub>-edge and i) Co K-edge XANES spectra. j) The mechanism diagram. Reproduced with permission.<sup>[100]</sup> Copyright 2018, Wiley-VCH. k) Polarization curves for OER. l) In situ electrochemical Raman spectra of 2D Ce-NiBDC/OG under different applied potentials. m) Scheme of the in situ phase transition from Ce-NiBDC/OG to Ce-NiOOH during the OER process. Reproduced with permission.<sup>[101]</sup> Copyright 2021, Royal Society of Chemistry.

exfoliated graphite nanosheets (Ce-NiBDC/OG) by a hydrothermal reaction.<sup>[101]</sup> The as-obtained Ce-NiBDC/OG delivered overpotentials of 265, 311, and 337 mV to attain the current densities of 10, 50, and 100 mA cm<sup>-2</sup> for OER in alkaline media (Figure 8k). Moreover, there are no obvious changes in current density after CP test at 10 mA cm<sup>-2</sup> for 10 h, suggesting the good stability of Ce-NiBDC/OG for OER. The in situ electrochemical Raman measurements were conducted and they indicated that there was an in situ transformation regarding the formation of Ce-NiBDC/OG into the Ce-NiOOH phase, which served as the real active sites for OER electrocatalysis (Figure 8l,m).

#### 4.3. 2D Heterostructures for Overall Water Splitting

It is imperative but challenging to develop high-performance HER and OER bifunctional electrocatalysts in the same electrolyte to simplify device fabrication.<sup>[102]</sup> 2D heterostructure

engineering is a desirable approach to preserve the intrinsic catalytic activities of each component and utilize the synergistic interfacial effects to reach good performance for both two half reactions (i.e., HER and OER) for overall water splitting.

For example, a dual-phase 2D Ni-Bi/meso-Ir heterostructure with amorphous nickel boron oxide layers anchored on the pore surface of mesoporous Ir nanosheets has been synthesized by a two-step wet-chemical reduction method (Figure 9a), which possessed abundant catalytically active heterointerfaces and boosted the exposure of the active site.<sup>[103]</sup> Owing to the superior and stable HER ( $\eta_{10} = 26.8$  mV) and OER ( $\eta_{10} = 250$  mV) performance, the Ni-Bi/meso-Ir catalyst was loaded on carbon fiber paper (CFP) to construct a two-electrode water electrolysis cell (Figure 9b). As a result, the LSV curves indicated that the cell with the Ni-Bi/meso-Ir required 1.55 V to reach a current density of 10 mA cm<sup>-2</sup> for water splitting, outperforming the coupled commercial Ir black|Pt/C catalysts (Figure 9c). The Ni-Bi/

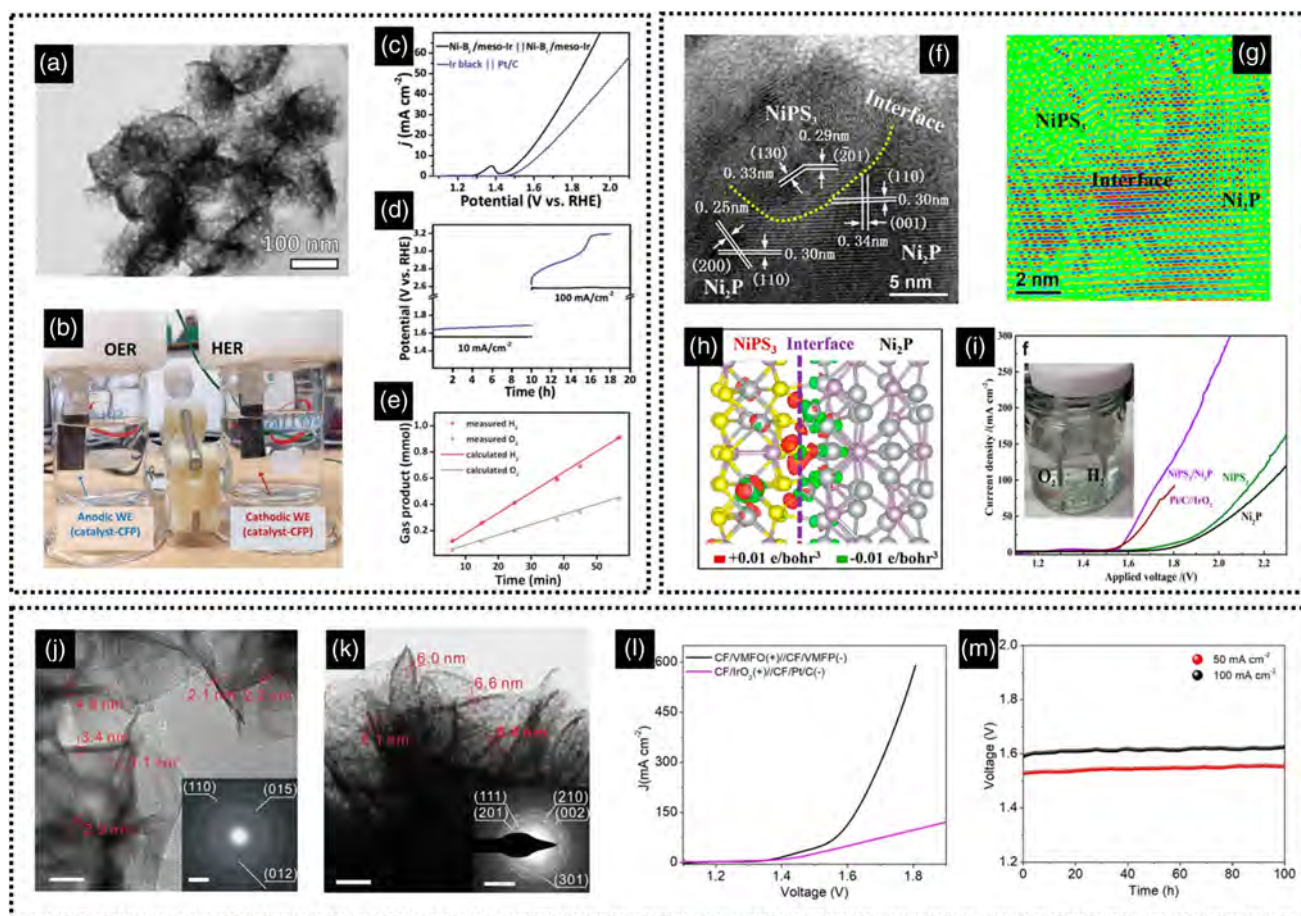


**Figure 9.** a) TEM image of 2D Ni–Bi/meso-Ir heterostructure. b) Photograph of the electrochemical overall water-splitting cell. c) LSV curves of Ni–Bi/meso-Ir heterostructures and Ir black–Pt/C coupled water electrolysis cell. d) The corresponding chronopotentiometry curves. e) The experimentally generated and theoretically calculated amounts of H<sub>2</sub> and O<sub>2</sub> on Ni–Bi/meso-Ir heterostructures. Reproduced with permission.<sup>[103]</sup> Copyright 2021, Wiley-VCH. f) HRTEM image and g) corresponding filtered HRTEM image by color. h) Distribution of charge density difference at the NiPS<sub>3</sub>/Ni<sub>2</sub>P interface. i) Polarization curves and reaction setup for overall water splitting. Reproduced with permission.<sup>[104]</sup> Copyright 2019, American Chemical Society. TEM images of j) 2D MoS<sub>2</sub>/FeCoNi(OH)<sub>x</sub> and k) MoS<sub>2</sub>/FeCoNiP<sub>x</sub>. l) Polarization curves for overall water splitting. m) Stability tests at 50 and 100 mA cm<sup>-2</sup> in a two-electrode configuration. Reproduced with permission.<sup>[106]</sup> Copyright 2021, Springer Nature.

meso-Ir-based device also exhibited better stability than that of commercial catalysts device at low (10 mA cm<sup>-2</sup>) and high (100 mA cm<sup>-2</sup>) current densities (Figure 9d). In addition, the produced H<sub>2</sub>:O<sub>2</sub> gas volume ratio in this electrolyzer was evaluated close to 2:1 with a faradaic efficiency of 98.1% and 97.4% for HER and OER, respectively (Figure 9e).

The synergistic interfacial effects contributing to overall water splitting were further investigated by intentional interfacial epitaxial engineering with the construction of 2D NiPS<sub>3</sub>/Ni<sub>2</sub>P heterostructures.<sup>[104]</sup> Specifically, Yan et al. achieved the epitaxial growth of Ni<sub>2</sub>P nanodomains on 2D NiPS<sub>3</sub> nanosheets exposed with (001) facets. The HRTEM image and the filtered HRTEM images by color demonstrated the nanoscale interfaces of NiPS<sub>3</sub> and Ni<sub>2</sub>P (Figure 9f,g). An obvious different charge density could be observed between NiPS<sub>3</sub> and Ni<sub>2</sub>P at the interface with the electron transferring from metallic Ni<sub>2</sub>P to NiPS<sub>3</sub>, which formed a built-in electric field to facilitate the electron transfer near the interfaces for electrocatalytic reaction (Figure 9h). In

this way, the 2D NiPS<sub>3</sub>/Ni<sub>2</sub>P heterostructures enabled the overall water splitting electrolyzer to achieve 50 mA cm<sup>-2</sup> at a lower bias of 1.65 V as compared with these of pristine NiPS<sub>3</sub> (2.02 V) and the benchmark Pt/C||IrO<sub>2</sub> electrocatalysts (1.69 V) (Figure 9i). In addition, such 2D NiPS<sub>3</sub>/Ni<sub>2</sub>P heterostructure-assembled electrolyzers could retain 10 mA cm<sup>-2</sup> over 10 h of continuous operation with a current retention of about 86%, which was much better than that of the cell with Pt/C and IrO<sub>2</sub>.

Based on the mechanism explorations to guide the rational design of high-performance 2D heterostructures, researchers are trying to further develop efficient bifunctional electrocatalysts to decrease the voltage at high current densities to meet the requirement of practical applications.<sup>[105]</sup> As illustrated in Figure 9j,k, Yu et al. designed the composite structure with the vertical graphene sheets (VGSs), MoS<sub>2</sub> nanosheets, and FeCoNi(OH)<sub>x</sub> or FeCoNiP<sub>x</sub> nanosheets stack on CFs.<sup>[106]</sup> The CF/VGSs/MoS<sub>2</sub>/FeCoNi(OH)<sub>x</sub> (CF/VMFO) showed an excellent OER performance in 1 M KOH solution with an overpotential of

225 mV at  $500 \text{ mA cm}^{-2}$  and a Tafel slope of  $29.2 \text{ mV dec}^{-1}$ . The CF/VGSs/  $\text{MoS}_2/\text{FeCoNiP}_x$  (CF/VMFP) was obtained by phosphating the  $\text{FeCoNi}(\text{OH})_x$  nanosheets, which exhibited good HER performance in 1 M KOH solution with an overpotential of 43 mV at  $10 \text{ mA cm}^{-2}$  and a Tafel slope of  $25.2 \text{ mV dec}^{-1}$ . When applying the CF/VMFO and CF/VMFP as anode and cathode for overall water splitting, a high current density of  $100 \text{ mA cm}^{-2}$  was delivered at 1.59 V with good stability for 100 h in 1 M KOH solution (Figure 9l,m).

Harvesting and converting energy from the environment by green energy systems to drive water splitting can decrease the external power consumption, which is a more cost-effective

approach for the practical application on a large scale. Thereinto, solar-driven water splitting can directly convert solar energy to hydrogen by a photovoltaic–electrochemical (PV–EC) device, which is regarded as an effective and environmentally friendly technology.<sup>[107]</sup>

Zhang et al. synthesized the heterogeneous bimetallic phosphide/sulfide nanosheet on NF (NiFeSP/NF) for high-performance electrocatalytic HER and OER activity in alkaline solution.<sup>[108]</sup> Combined with a Si solar cell, the bifunctional NiFeSP/NF electrocatalyst implemented unassisted solar-driven water splitting with a solar-to-hydrogen (STH) conversion efficiency of  $\approx 9.2\%$  (Figure 10a,b). In addition, under simulated

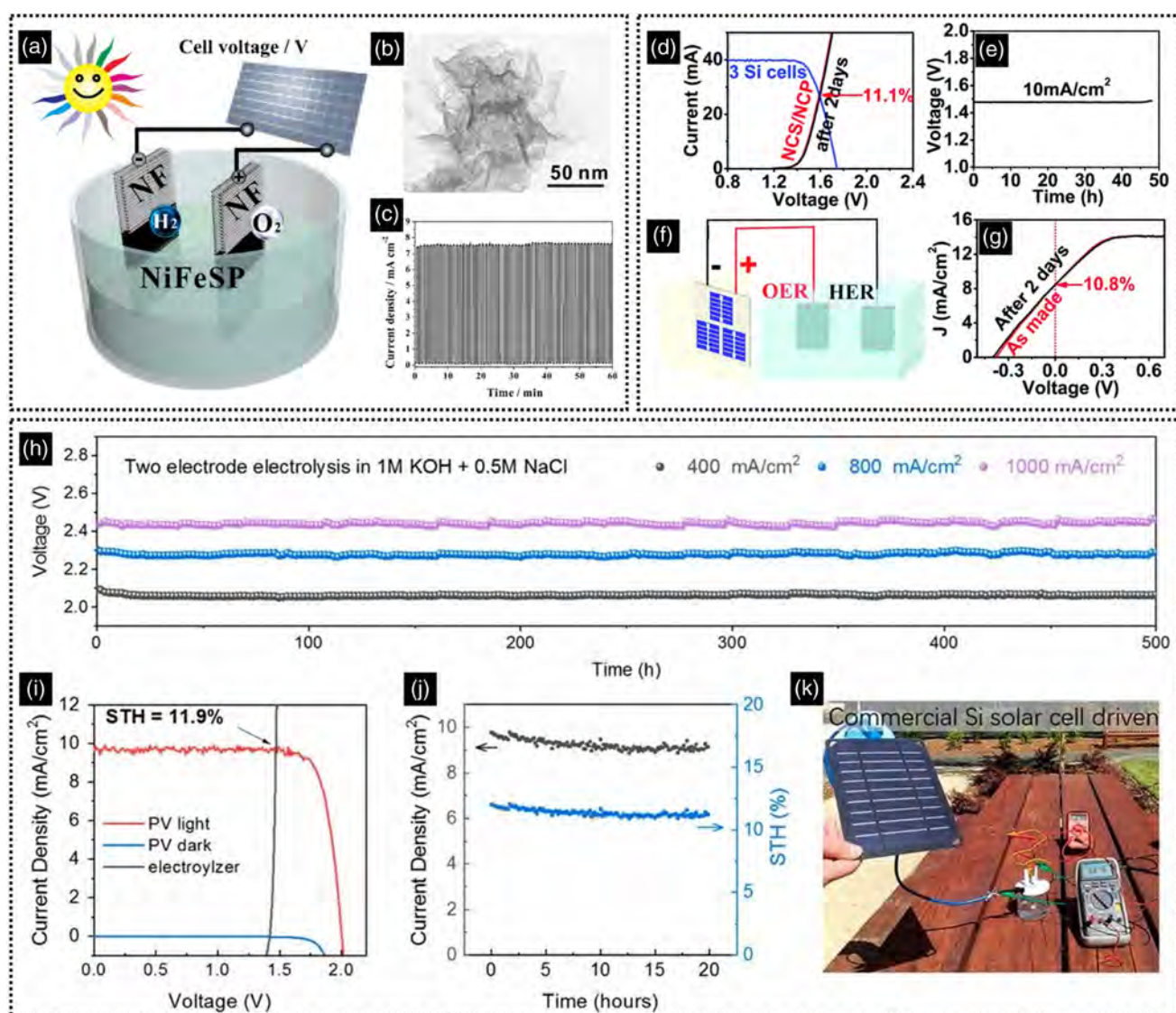


**Figure 10.** a) Schematic illustration of the solar-driven overall water-splitting system. b) TEM image of 2D NiFeSP. c) CP measurement under chopped simulated sunlight (AM 1.5G). Reproduced with permission.<sup>[108]</sup> Copyright 2017, American Chemical Society. d) Current–voltage ( $I$ – $V$ ) characteristics for overall electrocatalytic water splitting using NCS/NCP/NF. e) CP test at  $10 \text{ mA cm}^{-2}$ . f) Schematic illustration of three series-connected Si solar cell-driven water-splitting device. g)  $J$ – $V$  curves of water electrolysis under 1 sun illumination. Reproduced with permission.<sup>[109]</sup> Copyright 2018, Royal Society of Chemistry. h) Durability tests of the seawater splitting electrolyzer. i)  $J$ – $V$  curves of the seawater electrolyzer with two perovskite tandem cells under different conditions. j) Stability test. k) Photograph of a commercial Si solar cell-driven electrolysis. Reproduced with permission.<sup>[3]</sup> Copyright 2019, National Academy of Sciences, USA.

solar light illumination (AM 1.5G), the solar cells provided 1.6 V bias on the two-electrode electrolysis cell and generated a photocurrent density of  $7.5 \text{ mA cm}^{-2}$  with the repeated on-off cycles for 60 min, which yielded a Faradaic efficiency of 98.7% (Figure 10c). In addition, Shen et al. developed a bifunctional Ni-Co-S/Ni-Co-P bistratal electrocatalyst on NF.<sup>[109]</sup> When Ni-Co-S/Ni-Co-P was applied to overall water splitting as both cathode and anode, a small cell potential of 1.49 V could deliver  $10 \text{ mA cm}^{-2}$  and it could be sustained for about 48 h under the CP test (Figure 10d,e). Subsequently, three series-connected ordinary single-crystal Si solar cells with a total size of  $3 \text{ cm}^2$  were used to connect the electrocatalytic cell for unassisted water splitting (Figure 10f). The practical STH was tested to be 10.8%, which was close to the theoretical STH efficiency (11.1%, the cross point in Figure 10d). Furthermore, the current density–voltage ( $J$ - $V$ ) curve was unchanged after continuous solar-driven water splitting for 2 days, indicating the good stability of the electrocatalyst and the system (Figure 10g). These examples demonstrated that the 2D heterostructures have great potential in the solar-driven water-splitting application.

In addition, seawater is the most abundant water source on the Earth. Electrocatalysts developed for HER, OER, and overall water splitting using natural seawater or saline electrolyte have been increasingly reported.<sup>[110]</sup> As a typical example, Dai et al. presented an anode consisting of NiFe-LDH laminates coated on a nickel sulfide ( $\text{NiS}_x$ ) layer formed on porous NF ( $\text{NiFe}/\text{NiS}_x\text{-Ni}$ ).<sup>[3]</sup> The anodic activation process was applied and the activated/passivated  $\text{Ni}^3$  anode was obtained. Then, they paired  $\text{Ni}^3$  anode with a highly active Ni-NiO-Cr<sub>2</sub>O<sub>3</sub> HER cathode for two-electrode high-current electrolysis of alkaline seawater. It was found that such an electrolyzer displayed good durability at 400, 800, and 1,000  $\text{mA cm}^{-2}$  for 500 h in the simulated alkaline seawater (1 M KOH + 0.5 M NaCl) (Figure 10h). Furthermore, the same electrolyzer was connected in series with two perovskite solar cells ( $0.12 \text{ cm}^2$  masked area). As a result, under simulated sunlight illumination (AM 1.5G,  $100 \text{ mW cm}^{-2}$ ), an STH efficiency of  $11.9 \pm 0.1\%$  was achieved (Figure 10i). Moreover, this solar-driven seawater-splitting system could operate stably for 20 h without obvious STH decay (Figure 10j). Finally, they paired the seawater electrolyzer with a commercial Si solar cell (Renogy E.FLEX 5W, 5 V, 1 A) for a high-current test under real sunlight, obtaining  $\approx 880 \text{ mA}$  under a photovoltage of 2.75 V (Figure 10k). In this regard, the solar-driven seawater splitting can be a more sustainable way for energy conversion and utilization, in which the core concern for the electrocatalyst design (not limited to 2D heterostructures) is to sustain seawater splitting without chloride corrosion.

## 5. Conclusions and Perspectives

In this review, we highlight important recent advances in 2D heterostructures, from the various strategies for rational design and controllable synthesis to their efficient applications for electrocatalytic water splitting. This knowledge is expected for the design and synthesis of highly efficient 2D heterostructure catalysts for various energy storage and conversion applications. Compared with single 2D materials, the 2D heterostructures feature the structural advantages of 2D geometry (e.g., large surface area,

affluent active sites, fast electron transfer, and tunable electronic structures) and the component merits of hybrids (i.e., inherited individual properties and synergistic interface effects). These prepared 2D heterostructures have shown promising potential in energy-related applications including electrocatalytic HER, OER, and overall water splitting. Although significant achievements have been made in the construction and applications of 2D heterostructures, this research field still faces many challenges.

First of all, the wrinkle or buckle widely exists in freestanding 2D materials; however, related studies on the flatness of interfaces in 2D heterostructure have been sparse, which is critical to interface engineering and the modulation of catalytic performance. In addition, with the increasing complexity of the catalyst components, the reaction mechanism of 2D heterostructure during the electrocatalytic process still needs in-depth studies, especially for the OER. Based on the development of in situ or operando characterization methods, more advanced and sophisticated techniques, such as in situ Raman, in situ Fourier transform infrared (FTIR), in situ TEM, and in situ XANES spectroscopy, are highly required to monitor the real-time structural reconstruction and trace the real active sites for targeted reactions. It will provide a comprehensive understanding of the reaction kinetics and thermodynamic processes and offer useful guidance for rationally designing more efficient 2D heterostructures for electrocatalytic reactions. In addition, although DFT has provided insights into the reaction mechanism of well-determined active sites of single 2D nanomaterials based on the simplified models, it is more challenging to curate a definitive pathway for the 2D heterostructure systems with multifunctional active sites.

Second, the molding process or the assembly of 2D heterostructures into a real industrial electrode is an issue for the possibility of commercial applications. The freestanding 2D heterostructure nanosheets or nanoplates generally possess a loose structure and tend to aggregate at high temperatures or during the catalytic process with the desorption of adsorbed species or functional groups. The introduction of some conductive additives such as carbon black can not only improve the conductivity but also inhibit the stacking of 2D materials. On the other hand, there are typical examples as discussed above that the 2D heterostructures were in situ grown on metal foam and CFP, which exhibited good electrocatalytic activity and durability. Therefore, the growth of 2D heterostructures on well-conductive substrates directly served as electrodes which can provide a facile way to march closer to commercial applications.

Third, the catalytically active sites and intermediate adsorption are crucial to achieving high catalytic activity and better stability in the modification of intrinsic activity. Moving forward, it is of importance to pay attention to the improvement of electrocatalytic efficiency and durability at large current density. Because the current densities needed by industry are usually higher than 500 and 1000  $\text{mA cm}^{-2}$  for PEMs and AWEs,<sup>[111]</sup> the overpotentials for HER and OER at high current density (such as  $100 \text{ mA cm}^{-2}$ ,  $500 \text{ mA cm}^{-2}$ , and even  $1000 \text{ mA cm}^{-2}$ ) should be paid more efforts to decrease instead of just focusing on the overpotentials at  $10 \text{ mA cm}^{-2}$  as the standard for evaluating catalytic efficiency. Moreover, the stability test (CP or CA test) should be operated for a much longer time (such as 100 h, 500 h, and even 1000 h) at a high current density instead of just

operating for 10 or 24 h. In this respect, the effect of bubble dynamics or hydrophilicity–hydrophobicity deserves more attention in future research. First and foremost, the test setup needs to be standardized for the fair evaluation of catalyst performance under industrially relevant conditions.

Finally, for the solar-driven water-splitting technology to be effectively implemented, an STH of 10% as a large-scale commercialization standard or higher is desirable. To the best of our knowledge, the highest STH conversion efficiency was 30% to date, which was achieved by the InGaP/GaAs/GaInNAsSb triple-junction solar cell jointed with two series-connected polymer electrolyte membrane electrolyzers.<sup>[112]</sup> Currently, most of the reported PV-EC device systems generally encounter high Ohmic resistance, bulky connections, and a lack of highly integrated design, thus resulting in reduced efficiency. In addition, based on the calculated formula, the value of STH is equal to the ratio between chemical energy output and solar energy input. In this regard, lowering solution resistance, promoting the activity and stability of catalysts, and optimizing the mass transfer of the electrolysis device are the main feasible strategies to achieve higher STH efficiency when the efficiency of solar cells approximates the theoretical value.

2D heterostructures have shown great potential in the electrocatalytic water-splitting field, but the application-orientated research is just beginning. We believe that by understanding the catalytic nature of these materials with the assistance of in situ characterizations and DFT calculations and developing more rational preparation technologies for improving the overall efficiency and stability, the large-scale implementation of electrocatalytic applications will be achieved.

## Acknowledgements

This work was financially supported by the Environment and Conservation Fund of Hong Kong SAR, China (ECF 2020-13), and the City University of Hong Kong (project no. 9667227).

## Conflict of Interest

The authors declare no conflict of interest.

## Keywords

electrocatalyses, heterostructures, water splitting, 2D

Received: April 18, 2022

Revised: June 8, 2022

Published online: July 9, 2022

- [1] H. Zhang, W. Cheng, D. Luan, X. W. D. Lou, *Angew. Chem. Int. Ed.* **2021**, *60*, 13177.
- [2] P. Xiao, W. Chen, X. Wang, *Adv. Energy Mater.* **2015**, *5*, 1500985.
- [3] Y. Kuang, M. J. Kenney, Y. Meng, W.-H. Hung, Y. Liu, J. E. Huang, R. Prasanna, P. Li, Y. Li, L. Wang, M.-C. Lin, M. D. McGehee, X. Sun, H. Dai, *Proc. Natl. Acad. Sci.* **2019**, *116*, 6624.
- [4] X. Lu, S. Xie, H. Yang, Y. Tong, H. Ji, *Chem. Soc. Rev.* **2014**, *43*, 7581.
- [5] a) L. An, J. Feng, Y. Zhang, R. Wang, H. Liu, G.-C. Wang, F. Cheng, P. Xi, *Adv. Funct. Mater.* **2019**, *29*, 1805298; b) K. Jiang, M. Luo,

- M. Peng, Y. Yu, Y.-R. Lu, T.-S. Chan, P. Liu, F. M. F. de Groot, Y. Tan, *Nat. Commun.* **2020**, *11*, 2701.
- [6] L. Yu, Q. Zhu, S. Song, B. McElhenny, D. Wang, C. Wu, Z. Qin, J. Bao, Y. Yu, S. Chen, Z. Ren, *Nat. Commun.* **2019**, *10*, 5106.
- [7] Y. Shi, B. Zhang, *Chem. Soc. Rev.* **2016**, *45*, 1529.
- [8] L. An, C. Wei, M. Lu, H. Liu, Y. Chen, G. G. Scherer, A. C. Fisher, P. Xi, Z. J. Xu, C. H. Yan, *Adv. Mater.* **2021**, *33*, 2006328.
- [9] H. Song, M. Wu, Z. Tang, J. S. Tse, B. Yang, S. Lu, *Angew. Chem. Int. Ed.* **2021**, *60*, 7234.
- [10] L. Zhang, C. Lu, F. Ye, R. Pang, Y. Liu, Z. Wu, Z. Shao, Z. Sun, L. Hu, *Adv. Mater.* **2021**, *33*, 2007523.
- [11] S. Jiao, X. Fu, S. Wang, Y. Zhao, *Energy Environ. Sci.* **2021**, *14*, 1722.
- [12] S. Li, C. Cheng, A. Sagaltchik, P. Pachfule, C. Zhao, A. Thomas, *Adv. Funct. Mater.* **2019**, *29*, 1807419.
- [13] D. Zheng, L. Yu, W. Liu, X. Dai, X. Niu, W. Fu, W. Shi, F. Wu, X. Cao, *Cell Rep. Phys. Sci.* **2021**, *2*, 100443.
- [14] X. Chia, M. Pumera, *Nat. Catal.* **2018**, *1*, 909.
- [15] Q. Fu, X. Bao, *Chem. Soc. Rev.* **2017**, *46*, 1842.
- [16] J. Azadmanjiri, V. K. Srivastava, P. Kumar, J. Wang, A. Yu, *J. Mater. Chem. A* **2018**, *6*, 13509.
- [17] Y. Ge, Z. Shi, C. Tan, Y. Chen, H. Cheng, Q. He, H. Zhang, *Chem* **2020**, *6*, 1237.
- [18] M. Bat-Erdene, A. S. R. Bati, J. Qin, H. Zhao, Y. L. Zhong, J. G. Shapter, M. Batmunkh, *Adv. Funct. Mater.* **2021**, *32*, 2107280.
- [19] D. Deng, K. S. Novoselov, Q. Fu, N. Zheng, Z. Tian, X. Bao, *Nat. Nanotechnol.* **2016**, *11*, 218.
- [20] X. H. Wu, S. Zhou, Z. Y. Wang, J. S. Liu, W. Pei, P. J. Yang, J. J. Zhao, J. S. Qiu, *Adv. Energy Mater.* **2019**, *9*, 1901333.
- [21] X. Wu, X. Zhu, H. Tao, G. Wu, J. Xu, N. Bao, *Angew. Chem. Int. Ed.* **2021**, *60*, 21295.
- [22] L. Guo, Z. Yang, K. Marcus, Z. Li, B. Luo, L. Zhou, X. Wang, Y. Du, Y. Yang, *Energy Environ. Sci.* **2018**, *11*, 106.
- [23] G. Guan, M. Y. Han, *Adv. Sci.* **2019**, *6*, 1901837.
- [24] J. Su, G. D. Li, X. H. Li, J. S. Chen, *Adv. Sci.* **2019**, *6*, 1801702.
- [25] K. S. Novoselov, A. Mishchenko, A. Carvalho, A. H. Castro Neto, *Science* **2016**, *353*, 461.
- [26] Z. Sun, T. Ma, H. Tao, Q. Fan, B. Han, *Chem* **2017**, *3*, 560.
- [27] T. Zhang, Y. Wan, H. Xie, Y. Mu, P. Du, D. Wang, X. Wu, H. Ji, L. Wan, *J. Am. Chem. Soc.* **2018**, *140*, 7561.
- [28] Z. Wang, Z. Zeng, H. Wang, G. Zeng, P. Xu, R. Xiao, D. Huang, S. Chen, Y. He, C. Zhou, M. Cheng, H. Qin, *Coord. Chem. Rev.* **2021**, *439*, 213902.
- [29] J. D. Caldwell, I. Aharonovich, G. Cassaboiss, J. H. Edgar, B. Gil, D. N. Basov, *Nat. Rev. Mater.* **2019**, *4*, 552.
- [30] Y. Wang, L. Liu, T. Ma, Y. Zhang, H. Huang, *Adv. Funct. Mater.* **2021**, *31*, 2102540.
- [31] M. Zubair, M. M. Ul Hassan, M. T. Mehran, M. M. Baig, S. Hussain, F. Shahzad, *Int. J. Hydrogen Energy* **2022**, *47*, 2794.
- [32] A. Badreldin, A. E. Abusrafa, A. Abdel-Wahab, *ChemSusChem* **2021**, *14*, 10.
- [33] S. Anantharaj, S. Noda, V. R. Jothi, S. Yi, M. Driess, P. W. Menezes, *Angew. Chem. Int. Ed.* **2021**, *60*, 18981.
- [34] M. Cai, Q. Liu, Z. Xue, Y. Li, Y. Fan, A. Huang, M.-R. Li, M. Croft, T. A. Tyson, Z. Ke, G. Li, *J. Mater. Chem. A* **2020**, *8*, 190.
- [35] G. Bian, J. Yin, J. Zhu, *Small* **2021**, *17*, 2006043.
- [36] X. Zhao, T. Liu, Y.-L. Loo, *Adv. Mater.* **2022**, *34*, 2105849.
- [37] Z. Li, X. Zhang, H. Cheng, J. Liu, M. Shao, M. Wei, D. G. Evans, H. Zhang, X. Duan, *Adv. Energy Mater.* **2020**, *10*, 1900486.
- [38] G. H. Jeong, S. P. Sasikala, T. Yun, G. Y. Lee, W. J. Lee, S. O. Kim, *Adv. Mater.* **2020**, *32*, 1907006.
- [39] J. H. Kim, S. Y. Kim, Y. Cho, H. J. Park, H. J. Shin, S. Y. Kwon, Z. Lee, *Adv. Mater.* **2019**, *31*, 1807486.

- [40] Y. Liang, Y. Li, H. Wang, J. Zhou, J. Wang, T. Regier, H. Dai, *Nat Mater* **2011**, *10*, 780.
- [41] S. Zhao, J. Zhang, L. Fu, *Adv. Mater.* **2021**, *33*, 2005544.
- [42] a) L. Bai, X. Wang, S. Tang, Y. Kang, J. Wang, Y. Yu, Z.-K. Zhou, C. Ma, X. Zhang, J. Jiang, P. K. Chu, X.-F. Yu, *Adv. Mater.* **2018**, *30*, 1803641; b) Y. Abate, D. Akinwande, S. Gamage, H. Wang, M. Snure, N. Poudel, S. B. Cronin, *Adv. Mater.* **2018**, *30*, 1704749.
- [43] L. Zhang, Y. Zheng, J. Wang, Y. Geng, B. Zhang, J. He, J. Xue, T. Frauenheim, M. Li, *Small* **2021**, *17*, 2006730.
- [44] K. Gu, D. Wang, C. Xie, T. Wang, G. Huang, Y. Liu, Y. Zou, L. Tao, S. Wang, *Angew. Chem. Int. Ed.* **2021**, *60*, 20253.
- [45] L. Wang, Z. Zeng, W. Gao, T. Maxson, D. Raciti, M. Giroux, X. Pan, C. Wang, J. Greeley, *Science* **2019**, *363*, 870.
- [46] S. Gbadamasi, M. Mohiuddin, V. Krishnamurthi, R. Verma, M. W. Khan, S. Pathak, K. Kalantar-Zadeh, N. Mahmood, *Chem. Soc. Rev.* **2021**, *50*, 4684.
- [47] T. Dai, X. Zhang, M. Sun, B. Huang, N. Zhang, P. Da, R. Yang, Z. He, W. Wang, P. Xi, C. H. Yan, *Adv. Mater.* **2021**, *33*, 2102593.
- [48] T. A. Shifa, F. Wang, Y. Liu, J. He, *Adv. Mater.* **2019**, *31*, 1804828.
- [49] Z. Zou, Q. Wang, J. Yan, K. Zhu, K. Ye, G. Wang, D. Cao, *ACS Nano* **2021**, *15*, 12140.
- [50] J. Mei, T. Liao, Z. Sun, *Energy Environ. Mater.* **2021**, *5*, 115.
- [51] T. Zhou, C. Wu, Y. Wang, A. P. Tomsia, M. Li, E. Saiz, S. Fang, R. H. Baughman, L. Jiang, Q. Cheng, *Nat. Commun.* **2020**, *11*, 2077.
- [52] a) Q. Wang, D. O'Hare, *Chem. Rev.* **2012**, *112*, 4124-4155; b) D. Zhou, P. Li, X. Lin, A. McKinley, Y. Kuang, W. Liu, W.-F. Lin, X. Sun, X. Duan, *Chem. Soc. Rev.* **2021**, *50*, 87908817.
- [53] W. Ma, R. Ma, C. Wang, J. Liang, X. Liu, K. Zhou, T. Sasaki, *ACS Nano* **2015**, *9*, 1977.
- [54] X. Wang, R. K. M. Raghupathy, C. J. Querebillo, Z. Liao, D. Li, K. Lin, M. Hantusch, Z. Sofer, B. Li, E. Zschech, I. M. Weidinger, T. D. Kuhne, H. Mirhosseini, M. Yu, X. Feng, *Adv. Mater.* **2021**, *33*, 2008752.
- [55] Z. Yuan, J. Li, M. Yang, Z. Fang, J. Jian, D. Yu, X. Chen, L. Dai, *J. Am. Chem. Soc.* **2019**, *141*, 4972.
- [56] J. Nicks, K. Sasitharan, R. R. R. Prasad, D. J. Ashworth, J. A. Foster, *Adv. Funct. Mater.* **2021**, *31*, 2103723.
- [57] J. Guo, C. Y. Lin, Z. Xia, Z. Xiang, *Angew. Chem. Int. Ed.* **2018**, *57*, 12567.
- [58] Q. Quan, X. Lin, N. Zhang, Y. J. Xu, *Nanoscale* **2017**, *9*, 2398.
- [59] Y. Liu, J. Goebel, Y. Yin, *Chem. Soc. Rev.* **2013**, *42*, 2610.
- [60] Y. Xie, D. Kocaefe, C. Chen, Y. Kocaefe, *J. Nanomater.* **2016**, *2016*, 2302595.
- [61] B. Wang, C. Tang, H.-F. Wang, X. Chen, R. Cao, Q. Zhang, *Adv. Mater.* **2019**, *31*, 1805658.
- [62] Q. Quan, T. Zhang, C. Lei, B. Yang, Z. Li, J. Chen, C. Yuan, L. Lei, Y. Hou, *Nanoscale* **2019**, *11*, 22261.
- [63] X. J. Bai, X. Zhai, L. Y. Zhang, Y. Fu, W. Qi, *Matter* **2021**, *4*, 2919.
- [64] Z. Kou, T. Wang, Q. Gu, M. Xiong, L. Zheng, X. Li, Z. Pan, H. Chen, F. Verpoort, A. K. Cheetham, S. Mu, J. Wang, *Adv. Energy Mater.* **2019**, *9*, 1803768.
- [65] a) X. Xiao, H. Song, S. Lin, Y. Zhou, X. Zhan, Z. Hu, Q. Zhang, J. Sun, B. Yang, T. Li, L. Jiao, J. Zhou, J. Tang, Y. Gogotsi, *Nat. Commun.* **2016**, *7*, 11296; b) H. Jin, Q. Gu, B. Chen, C. Tang, Y. Zheng, H. Zhang, M. Jaroniec, S.-Z. Qiao, *Chem* **2020**, *6*, 2382.
- [66] C. Wu, J. Li, *ACS Appl. Mater. Interfaces* **2017**, *9*, 41314.
- [67] S.-H. Li, N. Zhang, X. Xie, R. Luque, Y.-J. Xu, *Angew. Chem. Int. Ed.* **2018**, *57*, 13082.
- [68] R. R. Poulakkandy, M. M. Menampambath, *Nanoscale Adv.* **2020**, *2*, 5015.
- [69] X. Huang, S. Li, Y. Huang, S. Wu, X. Zhou, S. Li, C. L. Gan, F. Boey, C. A. Mirkin, H. Zhang, *Nat. Commun.* **2011**, *2*, 292.
- [70] K. Tu, D. Tranca, F. Rodríguez-Hernández, K. Jiang, S. Huang, Q. Zheng, M.-X. Chen, C. Lu, Y. Su, Z. Chen, H. Mao, C. Yang, J. Jiang, H.-W. Liang, X. Zhuang, *Adv. Mater.* **2020**, *32*, 2005433.
- [71] C. L. Tan, J. Z. Chen, X. J. Wu, H. Zhang, *Nat. Rev. Mater.* **2018**, *3*, 17089.
- [72] H. Cheng, N. Yang, X. Liu, Y. Guo, B. Liu, J. Yang, Y. Chen, B. Chen, Z. Fan, Q. Lu, S. Yuan, J. Wang, L. Gu, H. Zhang, *Adv. Mater.* **2021**, *33*, 2007140.
- [73] P. C. Zhengwei Zhang, X. Duan, K. Zang, J. Luo, X. Duan, *Science* **2017**, *357*, 788.
- [74] M. Zhao, J. Chen, B. Chen, X. Zhang, Z. Shi, Z. Liu, Q. Ma, Y. Peng, C. Tan, X.-J. Wu, H. Zhang, *J. Am. Chem. Soc.* **2020**, *142*, 8953.
- [75] J. Wang, D. Liu, H. Huang, N. Yang, B. Yu, M. Wen, X. Wang, P. K. Chu, X. F. Yu, *Angew. Chem. Int. Ed.* **2018**, *57*, 2600.
- [76] Q. Quan, Z. Lai, Y. Bao, X. Bu, Y. Meng, W. Wang, T. Takahashi, T. Hosomi, K. Nagashima, T. Yanagida, C. Liu, J. Lu, J. C. Ho, *Small* **2021**, *17*, 2006860.
- [77] T. Yang, B. Zheng, Z. Wang, T. Xu, C. Pan, J. Zou, X. Zhang, Z. Qi, H. Liu, Y. Feng, W. Hu, F. Miao, L. Sun, X. Duan, A. Pan, *Nat. Commun.* **2017**, *8*, 1906.
- [78] X. Wang, Z. Wang, J. Zhang, X. Wang, Z. Zhang, J. Wang, Z. Zhu, Z. Li, Y. Liu, X. Hu, J. Qiu, G. Hu, B. Chen, N. Wang, Q. He, J. Chen, J. Yan, W. Zhang, T. Hasan, S. Li, H. Li, H. Zhang, Q. Wang, X. Huang, W. Huang, *Nat. Commun.* **2018**, *9*, 3611.
- [79] Y. Fang, Y. Xue, L. Hui, H. Yu, Y. Liu, C. Xing, F. Lu, F. He, H. Liu, Y. Li, *Nano Energy* **2019**, *59*, 591.
- [80] L. Li, D. Yu, P. Li, H. Huang, D. Xie, C.-C. Lin, F. Hu, H.-Y. Chen, S. Peng, *Energy Environ. Sci.* **2021**, *14*, 6419.
- [81] C. Zeng, F. Xie, X. Yang, M. Jaroniec, L. Zhang, S. Z. Qiao, *Angew. Chem. Int. Ed.* **2018**, *57*, 8540.
- [82] B. Xu, H. Chakraborty, V. K. Yadav, Z. Zhang, M. L. Klein, S. Ren, *Nat. Commun.* **2017**, *8*, 312.
- [83] S.-H. Li, M.-Y. Qi, Y.-Y. Fan, Y. Yang, M. Anpo, Y. M. A. Yamada, Z.-R. Tang, Y.-J. Xu, *Appl. Catal., B* **2021**, *292*, 120157.
- [84] C. Tan, X. Cao, X.-J. Wu, Q. He, J. Yang, X. Zhang, J. Chen, W. Zhao, S. Han, G.-H. Nam, M. Sindoro, H. Zhang, *Chem. Rev.* **2017**, *117*, 6225.
- [85] C.-T. Dinh, A. Jain, F. P. G. de Arquer, P. De Luna, J. Li, N. Wang, X. Zheng, J. Cai, B. Z. Gregory, O. Voznyy, B. Zhang, M. Liu, D. Sinton, E. J. Crumlin, E. H. Sargent, *Nat. Energy* **2019**, *4*, 107.
- [86] a) A. Kumar, V. Q. Bui, J. Lee, A. R. Jadhav, Y. Hwang, M. G. Kim, Y. Kawazoe, H. Lee, *ACS Energy Lett.* **2021**, *6*, 354; b) Z. Li, Y. Feng, Y.-L. Liang, C.-Q. Cheng, C.-K. Dong, H. Liu, X.-W. Du, *Adv. Mater.* **2020**, *32*, 1908521.
- [87] S. Ye, W. Xiong, P. Liao, L. Zheng, X. Ren, C. He, Q. Zhang, J. Liu, *J. Mater. Chem. A* **2020**, *8*, 11246.
- [88] N. Cheng, S. Stambula, D. Wang, M. N. Banis, J. Liu, A. Riese, B. Xiao, R. Li, T.-K. Sham, L.-M. Liu, G. A. Botton, X. Sun, *Nat. Commun.* **2016**, *7*, 13638.
- [89] S. W. Jang, S. Dutta, A. Kumar, Y.-R. Hong, H. Kang, S. Lee, S. Ryu, W. Choi, I. S. Lee, *ACS Nano* **2020**, *14*, 10578.
- [90] Q. Quan, X. Bu, D. Chen, F. Wang, X. Kang, W. Wang, Y. Meng, S. Yip, C. Liu, J. C. Ho, *J. Mater. Chem. A* **2022**, *10*, 3953.
- [91] Y. Wang, K. Xu, Z. Zhu, W. Guo, T. Yu, M. He, W. Wei, T. Yang, *Chem. Commun.* **2021**, *57*, 1368.
- [92] J. Cai, Y. Song, Y. Zang, S. Niu, Y. Wu, Y. Xie, X. Zheng, Y. Liu, Y. Lin, X. Liu, G. Wang, Y. Qian, *Sci. Adv.* **2020**, *6*, eaaw8113.
- [93] C. Yang, R. Zhao, H. Xiang, J. Wu, W. Zhong, W. Li, Q. Zhang, N. Yang, X. Li, *Adv. Energy Mater.* **2020**, *10*, 2002260.
- [94] H. Wang, J. Li, K. Li, Y. Lin, J. Chen, L. Gao, V. Nicolosi, X. Xiao, J.-M. Lee, *Chem. Soc. Rev.* **2021**, *50*, 1354.
- [95] a) Y. Gu, A. Wu, Y. Jiao, H. Zheng, X. Wang, Y. Xie, L. Wang, C. Tian, H. Fu, *Angew. Chem. Int. Ed.* **2020**, *60*, 6673; b) G. Guan, M.-Y. Han, *Adv. Sci.* **2019**, *6*, 1901837.
- [96] L. Wang, Z. Li, K. Wang, Q. Dai, C. Lei, B. Yang, Q. Zhang, L. Lei, M. K. H. Leung, Y. Hou, *Nano Energy* **2020**, *74*, 104850.

- [97] D. Liu, Q. Lv, S. Lu, J. Fang, Y. Zhang, X. Wang, Y. Xue, W. Zhu, Z. Zhuang, *Nano Lett.* **2021**, 21, 2809.
- [98] X. Hu, S. Zhang, J. Sun, L. Yu, X. Qian, R. Hu, Y. Wang, H. Zhao, J. Zhu, *Nano Energy* **2018**, 56, 109.
- [99] M.-X. Chen, M. Zhu, M. Zuo, S.-Q. Chu, J. Zhang, Y. Wu, H.-W. Liang, X. Feng, *Angew. Chem. Int. Ed.* **2020**, 59, 1627.
- [100] Y. Zhang, C. Wu, H. Jiang, Y. Lin, H. Liu, Q. He, S. Chen, T. Duan, L. Song, *Adv. Mater.* **2018**, 30, 1707522.
- [101] F. Cheng, Z. Li, L. Wang, B. Yang, J. Lu, L. Lei, T. Ma, Y. Hou, *Mater. Horiz.* **2021**, 8, 556.
- [102] a) Y. Zhao, J. Zhang, Y. Xie, B. Sun, J. Jiang, W.-J. Jiang, S. Xi, H. Y. Yang, K. Yan, S. Wang, X. Guo, P. Li, Z. Han, X. Lu, H. Liu, G. Wang, *Nano Lett.* **2021**, 21, 823; b) F. Yu, H. Zhou, Y. Huang, J. Sun, F. Qin, J. Bao, W. A. Goddard, S. Chen, Z. Ren, *Nat. Commun.* **2018**, 9, 2551.
- [103] Z. Wang, Y. Wu, K. Xu, L. Jiang, J. Sun, G. Cai, G. Li, B. Y. Xia, H. Liu, *Adv. Funct. Mater.* **2021**, 31, 2104732.
- [104] Q. Liang, L. Zhong, C. Du, Y. Luo, J. Zhao, Y. Zheng, J. Xu, J. Ma, C. Liu, S. Li, Q. Yan, *ACS Nano* **2019**, 13, 7975.
- [105] Y. Luo, Z. Zhang, M. Chhowalla, B. Liu, *Adv. Mater.* **2021**, 34, 2108133.
- [106] X. Ji, Y. Lin, J. Zeng, Z. Ren, Z. Lin, Y. Mu, Y. Qiu, J. Yu, *Nat. Commun.* **2021**, 12, 1380.
- [107] R. Lin, H. Lei, D. Ruan, K. Jiang, X. Yu, Z. Wang, W. Mai, H. Yan, *Nano Energy* **2019**, 56, 82.
- [108] Y. Xin, X. Kan, L.-Y. Gan, Z. Zhang, *ACS Nano* **2017**, 11, 10303.
- [109] X. Zhou, J. Zhou, G. Huang, R. Fan, S. Ju, Z. Mi, M. Shen, *J. Mater. Chem. A* **2018**, 6, 20297.
- [110] L. Z. Zhuang, J. K. Li, K. Y. Wang, Z. H. Li, M. H. Zhu, Z. Xu, *Adv. Funct. Mater.* **2022**, 2201127.
- [111] C. Zhang, Y. Luo, J. Tan, Q. Yu, F. Yang, Z. Zhang, L. Yang, H.-M. Cheng, B. Liu, *Nat. Commun.* **2020**, 11, 3724.
- [112] J. Jia, L. C. Seitz, J. D. Benck, Y. Huo, Y. Chen, J. W. D. Ng, T. Bilir, J. S. Harris, T. F. Jaramillo, *Nat. Commun.* **2016**, 7, 13237.



**Quan Quan** is a Ph.D. candidate in the Department of Materials Science and Engineering at the City University of Hong Kong. Her research interests mainly focus on the synthesis of nanostructural catalysts for applications in electrocatalysis and related interdisciplinary sustainable chemistry.



**Johnny C. Ho** is a professor of Materials Science and Engineering at the City University of Hong Kong. He received his B.S. in chemical engineering and his M.S. and Ph.D. in materials science and engineering from the University of California, Berkeley, in 2002, 2005, and 2009, respectively. From 2009 to 2010, he was a postdoctoral research fellow in the Nanoscale Synthesis and Characterization Group at Lawrence Livermore National Laboratory. His research interests focus on synthesis, characterization, integration, and device applications of nanoscale materials for various technological applications, including nanoelectronics, sensors, and energy harvesting.